

# Separation of Specific Single-Enantiomer Single-Wall Carbon Nanotubes in the Large-Diameter Regime

Han Li,<sup>\*,†</sup> Georgy Gordeev,<sup>‡</sup> Oisín Garrity,<sup>‡</sup> Naga Anirudh Peyyety,<sup>†,§</sup> Pranaav Balaji Selvasundaram,<sup>†,§</sup> Simone Dehm,<sup>†</sup> Ralph Krupke,<sup>†,§</sup> Sofie Cambré,<sup>||</sup> Wim Wenseleers,<sup>||</sup> Stephanie Reich,<sup>‡</sup> Ming Zheng,<sup>⊥</sup> Jeffrey A. Fagan,<sup>\*,⊥</sup> and Benjamin S. Flavel<sup>\*,†</sup>

<sup>†</sup>Institute of Nanotechnology, Karlsruhe Institute of Technology, Karlsruhe 76021, Germany

<sup>‡</sup>Department of Physics, Freie Universität Berlin, Berlin 14195, Germany

<sup>§</sup>Institute of Materials Science, Technische Universität Darmstadt, Darmstadt 64287, Germany

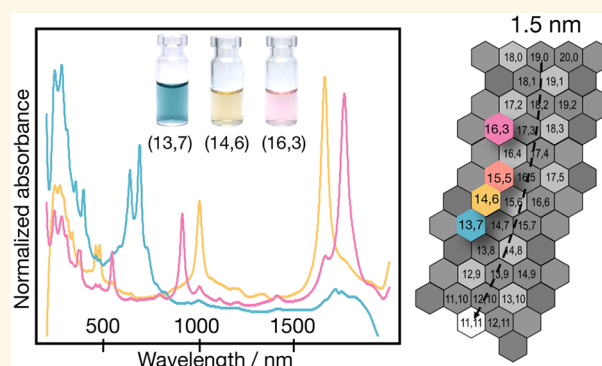
<sup>||</sup>Physics Department, University of Antwerp, Antwerp 2020, Belgium

<sup>⊥</sup>Materials Science and Engineering Division, National Institute of Standards and Technology, Gaithersburg, Maryland 20899, United States

## Supporting Information

**ABSTRACT:** The enantiomer-level isolation of single-walled carbon nanotubes (SWCNTs) in high concentration and with high purity for nanotubes greater than 1.1 nm in diameter is demonstrated using a two-stage aqueous two-phase extraction (ATPE) technique. In total, five different nanotube species of  $\sim 1.41$  nm diameter are isolated, including both metallics and semiconductors. We characterize these populations by absorbance spectroscopy, circular dichroism spectroscopy, resonance Raman spectroscopy, and photoluminescence mapping, revealing and substantiating mod-dependent optical dependencies. Using knowledge of the competitive adsorption of surfactants to the SWCNTs that controls partitioning within the ATPE separation, we describe an advanced acid addition methodology that enables the fine control of the separation of these select nanotubes. Furthermore, we show that endohedral filling is a previously unrecognized but important factor to ensure a homogeneous starting material and further enhance the separation yield, with the best results for alkane-filled SWCNTs, followed by empty SWCNTs, with the intrinsic inhomogeneity of water-filled SWCNTs causing them to be worse for separations. Lastly, we demonstrate the potential use of these nanotubes in field-effect transistors.

**KEYWORDS:** chiral sorting, ATPE, SWCNT, dextran, PEG, polymer



The use of single-walled carbon nanotubes (SWCNTs) in next-generation electronics,<sup>1</sup> energy applications,<sup>2</sup> biosensing,<sup>3</sup> and quantum information<sup>4</sup> requires the development of protocols for enrichment by their chiral lattice structure (i.e., their species and enantiomeric handedness). Much effort, including a combination of both selective growth<sup>5</sup> and a wealth of processing techniques,<sup>6,7</sup> has enabled the preparation of SWCNT populations with tailored diameter,<sup>8</sup> length,<sup>9</sup> wall number and wall type,<sup>10,11</sup> electronic properties,<sup>12</sup> and chirality (species).<sup>13</sup> Notably, the development of  $W_6Co_7$ ,<sup>14</sup>  $Mo_2C$ , and  $WC$  catalysts<sup>15</sup> and separation methods such as polymer extraction,<sup>16–19</sup> gel permeation chromatography,<sup>20–26</sup> density gradient ultracentrifugation (DGU),<sup>12,27–30</sup> aqueous two-phase extraction (ATPE),<sup>31–33</sup>

and selective DNA strands<sup>13</sup> have all allowed for rapid progress in this area. In the small SWCNT diameter regime ( $D_t = 0.8$  to 1 nm), these techniques have now made accessible a vast library of chirality-pure SWCNTs and have even allowed for the discrimination of single enantiomers.<sup>30,34–38</sup> Regrettably, however, for SWCNT diameters larger than 1 nm, the list of isolated single-chiral species is dramatically smaller, and enantiomer enrichment has yet to be demonstrated.<sup>39</sup>

The reasons for the lack of resolution among the larger diameter nanotube species are manifold but are chiefly due to

**Received:** October 18, 2019

**Accepted:** November 19, 2019

**Published:** November 19, 2019

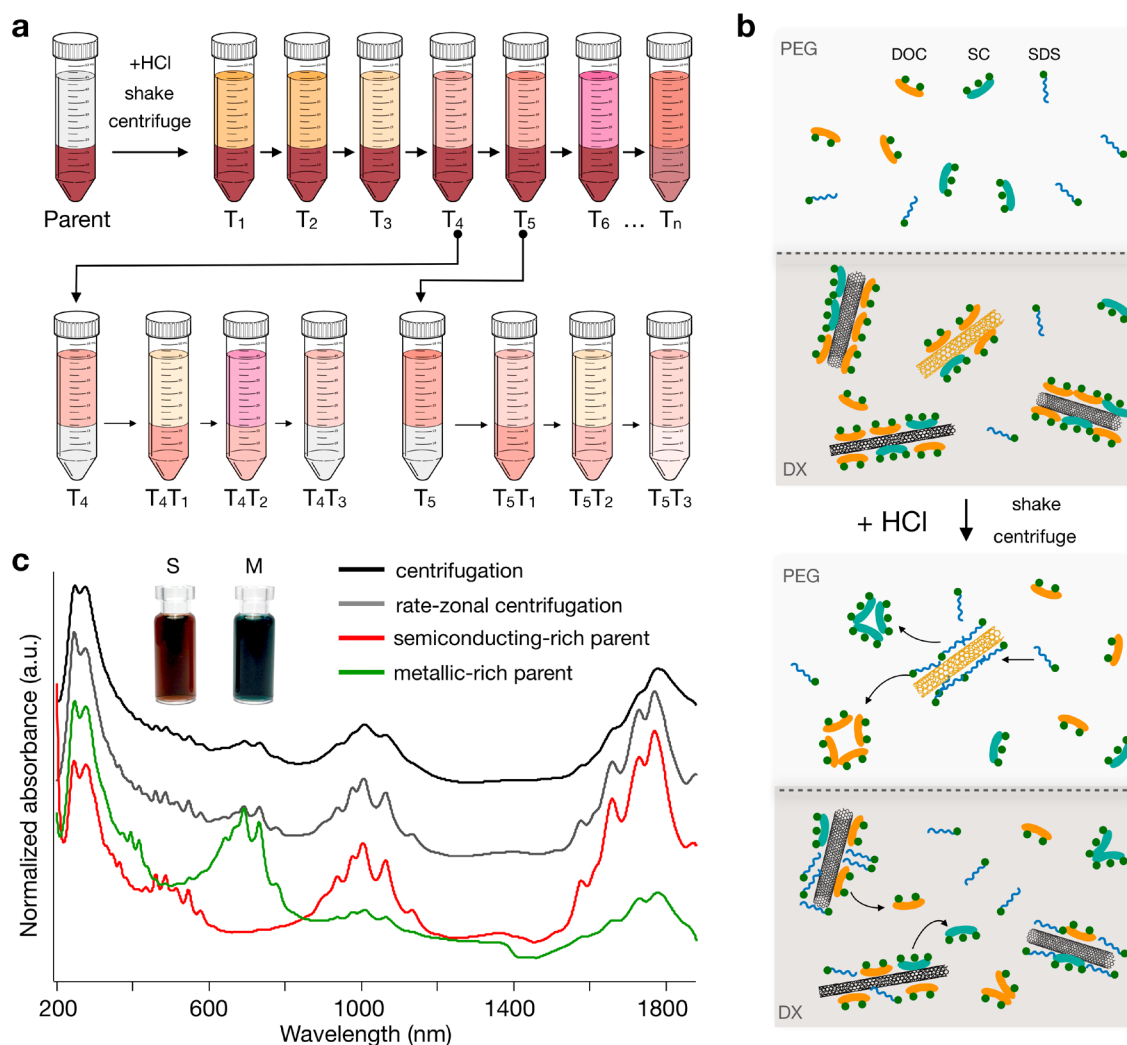


**Figure 1.** Illustration of the aqueous two-phase separation and preparation of the parent SWCNT suspension for enantiomer sorting. (a) A two-phase extraction cascade consisting of two stages is used to separate the parent suspension into  $(n,m)$  pure fractions. In stage 1, the parent (initially located in the bottom phase) is split into sequential top-phase fractions ( $T_1$ – $T_n$ ) by adding increasing volumes of HCl. Between each acid addition, the top phase ( $T_n$ ) is extracted and replaced by a fresh mimic top phase. In stage 2, a top-phase fraction ( $T_n$ ) is added to fresh bottom phase to re-establish the two-phase system before repeating the sequential addition of HCl to obtain new top-phase fractions ( $T_nT_m$ ). (b) Proposed mechanism for pH-driven ATPE separation of large-diameter ( $\sim 1.5$  nm) SWCNTs. Before the addition of HCl, the SWCNTs are mainly wrapped in DOC/SC, and their surfactant shell is chirality-dependent. After the addition of HCl, the protonation of the carboxylic acid on DOC/SC leads to an increase in their aggregation number and the formation of surfactant aggregates in solution. Consequently, DOC/SC is replaced by SDS around the nanotube, and this occurs in a chirality-dependent manner. This process drives the nanotubes into the PEG phase. (c)  $C_{16}H_{34}@EA$  SWCNTs are dispersed in  $H_2O$  via sonication in 2% DOC, followed by centrifugation, rate-zonal centrifugation, and electronic-type separation to obtain two parent suspensions.

the increasing number of species with similar diameters and difficulties in controlling the catalyst size during growth.<sup>5</sup> This leads to both a greater number of species in larger diameter raw materials and each  $(n,m)$  comprising a commensurately lower mass fraction of the total. For example, there are  $\sim 32$  possible chiral species with a diameter of 0.6 to 1 nm (carbon-center-to-carbon-center definition), whereas there are close to 150 species with a diameter between 1 and 2 nm.<sup>40</sup> This theoretical increase is matched in experimental reports of detectable SWCNT species from various sources. van Bezouw et al.<sup>41</sup> detected up to 34 different semiconducting  $(n,m)$  species in plasma torch (PT) synthesis and laser vaporization (LV) raw soot materials ( $D_t \approx 0.945$  to 1.53 nm) compared with CoMoCAT-SG65i ( $D_t \approx 0.69$  to 0.92 nm) with only 17 species.<sup>42</sup> Both measures likely undercounted small fractional population  $(n,m)$  species interdigitated with the observed

species and also disregarded the added complexity of most observed species being divided between both left- and right-hand twisted enantiomers.

As a further difficulty, large-diameter raw soot tends to have less dispersible SWCNT content on a mass powder basis ( $\sim 70\%$ ) relative to its small-diameter counterparts (up to  $\sim 95\%$ ). Consequently, significantly more raw material is required to obtain an appreciable quantity of any one species from a separation. Combined with the reduced mass of any given  $(n,m)$  species per mass, it is also generally accepted that the chemical differences between  $(n,m)$  species decrease with increasing diameter, as both the difference in band levels between the metallic (m) and semiconducting (s) subpopulations is reduced and, within these subpopulations, the variations in bond strain and the diameters between adjacent  $(n,m)$  species are decreased.<sup>39</sup> These factors are likely to

reduce the structural differences in adsorbed dispersant coatings around each  $(n,m)$  species, which are especially important for separation protocols reliant upon surfactant-wrapped SWCNTs.<sup>39,43</sup>

A large SWCNT diameter is also associated with an increased technical difficulty for characterization. Indeed, few laboratories are equipped with the appropriate combination of detectors and tunable light sources to measure Raman and photoluminescence excitation (PLE) contour maps of CNTs with a diameter  $>1.4$  nm. Even for standard absorbance spectroscopy the spectral position of the first-order semi-conducting optical transition ( $S_{11} \approx 1400\text{--}2000$  nm) becomes coincident with absorbance features of  $\text{H}_2\text{O}$ , adding technical difficulty and cost to characterization. This is in contrast with small-diameter SWCNTs, which exhibit all of their optical transitions at  $<1400$  nm and thus can be observed through standard cuvettes, at lower SWCNT concentrations, and without  $\text{D}_2\text{O}$  exchange. For large-diameter SWCNTs (generally  $>1.6$  nm), the entire aqueous separation must either be performed using costly  $\text{D}_2\text{O}$  or solvent-exchange processes must be employed to allow for the observation of the  $S_{11}$  features.<sup>39</sup> Lastly, for open-ended nanotubes exposed to an aqueous environment, the signal-to-noise ratio from all of the optical characterization methods is reduced due to the dramatic broadening and quenching of optical features for water-filled SWCNTs.<sup>44–46</sup>

Despite the associated challenges, electronically defined, single-chirality, large-diameter SWCNTs are expected to be important building blocks for research and both electronic and photonic applications. For example, the performance of SWCNT field-effect transistors (SWCNT-FETs) was shown to be enhanced when using SWCNTs with a diameter  $>1.2$  nm due to a reduction of the Schottky barrier height<sup>47</sup> and the quadratic dependence of carrier mobility on the SWCNT diameter.<sup>47</sup> Solar cells and light sensors<sup>48</sup> will also benefit from light absorption deeper in the infrared and the low sheet resistance of films from large-diameter SWCNTs.<sup>48,49</sup> Type-II heterojunctions have already been shown to form between large-diameter  $s$ -SWCNTs ( $D_t \approx 1.665$  nm) and fullerene acceptors with high electron affinity,<sup>49</sup> and species such as (16,3), (15,5) (14,3), and (13,5) ( $D_t \approx 1.25\text{--}1.43$  nm)<sup>48</sup> are predicted to have the least overlap with the solar spectrum in the region of silicon absorption, an important property for their use as a conductive layer in Si-CNT solar cells.<sup>48</sup> In emerging photonic technologies, the infrared position of  $S_{11}$  and the generation of controlled emissive defect states<sup>50</sup> make large-diameter SWCNTs technologically attractive for electrically driven on-chip single-photon emitters in telecommunications.<sup>4</sup> Moreover, the endohedral volume of large-diameter SWCNTs also provide a scaffold for advanced 1D heterostructures such as dye molecules to create new nanoprobe for bioimaging,<sup>51</sup> nonlinear optical phenomena,<sup>52</sup> and energy-transfer processes.<sup>41</sup>

The process we use to isolate the large-diameter SWCNT species and enantiomers in this contribution is ATPE. ATPE provides key advantages for the isolation of SWCNTs in the large-diameter regime such as the ability to process concentrated SWCNT dispersions, ready scale-up through the use of larger containers, the tailorable control of conditions affecting partitioning, and even easy concentration of final products via partition into a small volume of the opposing phase<sup>39,53</sup> to facilitate solvent exchange and reduce material expense. The true advantage of ATPE, however, is that it is

sensitive to extremely small differences in the surfactant shell around an SWCNT,<sup>54</sup> providing the necessary resolution in the large-diameter regime. In this regard, strong oxidants, reductants,<sup>55</sup> salts,<sup>54</sup> temperature,<sup>54</sup> and surfactant concentration<sup>39</sup> have been shown to modulate the composition and density of the surfactant shell and enable separation. Most recently, we have demonstrated the use of pH to control ATPE,<sup>56</sup> which adds the ability to modulate species-based SWCNT partitioning while the global surfactant composition remains (nearly) fixed. In this contribution, we combine this advance with the use of alkane-filled SWCNTs for the large-diameter nanotubes to improve the characterizability of the optical properties and simplify the spectroscopic analysis.<sup>44</sup> We now further develop the use of acid in the ATPE system to extract large-diameter SWCNT enantiomers.

## RESULTS AND DISCUSSION

The acid-addition ATPE separation approach is illustrated in Figure 1a. A parent SWCNT suspension is added to a self-separating polyethylene glycol (PEG)/dextran (DX) two-phase system, resulting in a known global surfactant concentration(s) and typically partitioning the SWCNTs into the bottom phase. For competition between bile salts and surfactants such as SDS, the addition of HCl aliquots changes the equilibrium composition of the adsorbed interfacial layer on the SWCNTs in an orderly fashion and drives those SWCNTs whose interfaces change with the acid addition to partition from the bottom DX to the top PEG phase.<sup>56</sup> The resultant SWCNT-containing PEG phase is then removed and replaced with a clean mimic PEG phase (containing a surfactant composition at concentrations truly mimicking the original two-phase system), and the process is repeated to obtain a series of stage-1 fractions ( $T_1\text{--}T_n$ ), with more total acid added for each new top phase. These fractions are either used directly ( $T_1$ ,  $T_2$ ,  $T_3$ ,  $T_6$ ) or recombined ( $T_4$ ,  $T_5$ ) with fresh DX mimic phase in a cascade series to generate stage-2 fractions (e.g.,  $T_4T_1$ ,  $T_4T_2$ ,  $T_4T_3$ ). Although further stages are possible, the cascade was intentionally restricted to two stages to impart an inherent simplicity to the approach and improve the reproducibility for others in the field. The important concept is that in a pH-driven ATPE approach, the global surfactant concentrations do not change, only the distribution of the surfactants between the SWCNT surface and the soluble/insoluble molecules in solution, and thus it is highly important that appropriate conditions are found prior to separation.

**Surfactant Conditions.** Surfactant concentrations must be used that ensure discriminable differences in the surfactant shells of different  $(n,m)$  species with enough sensitivity to achieve separation within a limited number of steps. In the past, Li et al.<sup>56</sup> used a sodium deoxycholate (DOC)/sodium dodecyl sulfate (SDS) cosurfactant mixture of 0.05% DOC/0.5% SDS to separate small-diameter ( $D_t \approx 0.9$  nm) SWCNTs in one to three steps, Fagan et al.<sup>39,42</sup> used combinations from 0.04 to 0.15% DOC with 0.5 to 1.2% SDS, and Subbaiyan et al.<sup>54</sup> showed that the addition of sodium cholate (SC) (0.05% DOC/1 to 2% SDS/0.5% SC) further enhanced the purity of specific small-diameter chiralities and allowed for the number of experimental steps to be reduced to 2. These authors discussed the importance of more DOC and less SDS for larger diameter SWCNTs along with the importance of SC to introduce a selectivity to the chiral angle, as first demonstrated for specific small diameters<sup>54</sup> or enantiomeric types.<sup>42,56</sup>

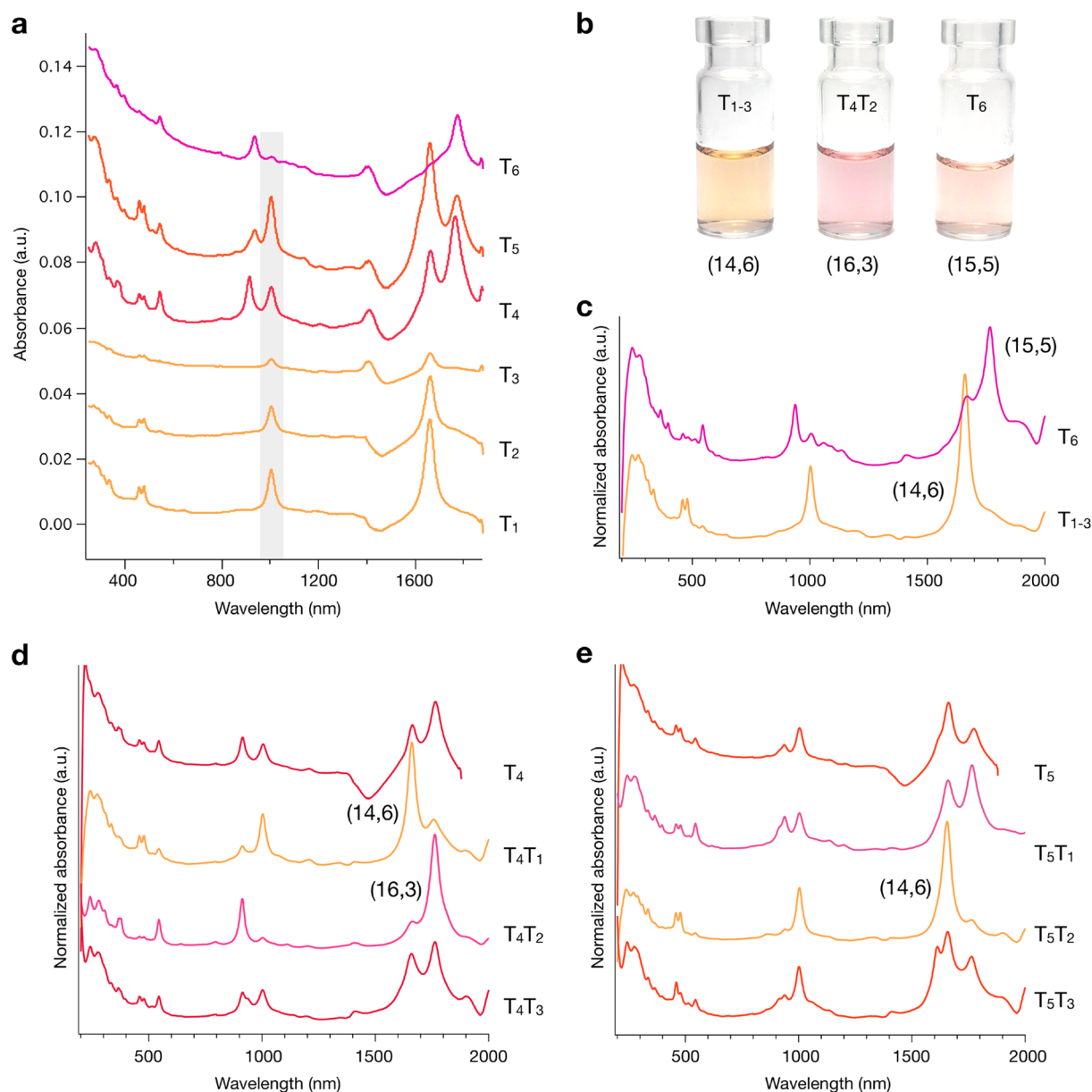


**Figure 2.** Separation of the  $C_{16}H_{34}@EA$  semiconducting parent. (a) Absorption spectra of stage-1 fractions in  $H_2O$  ( $T_1$ – $T_6$ ).  $T_1$ – $T_3$  and  $T_6$  contained single-chirality SWCNTs after stage 1, and these were concentrated and transferred to  $D_2O$ . (b) Photograph of the  $(n,m)$  pure fractions obtained and (c) their absorption spectra.  $T_4$  and  $T_5$  were further processed in stage 2, and the corresponding spectra are shown in panels d and e, respectively. To improve the spectral clarity, all stage-2 fractions were concentrated and transferred to  $D_2O$ . Note: The absorbance of water shifts with pH, and the scattering in the samples increases with increasing acid content. Therefore, all fractions measured in  $H_2O$  contain a water-related component at 1350–1450 nm and are responsible for the negative absorbance distortions in samples. The increased short wavelength absorbance below 500 nm in  $T_5$  and  $T_6$  is due to scattering.  $T_{1-3}$  was assigned to (14,6) with a diameter of 1.411 nm ( $S_{11} = 1660$  nm,  $S_{22} = 1003$  nm,  $S_{33} = 479$  nm,  $S_{44} = 459$  nm).  $T_6$  was assigned to (15,5) with a diameter of 1.431 nm ( $S_{11} = 1766$  nm,  $S_{22} = 938$  nm,  $S_{33} = 544$  nm,  $S_{44} = 365$  nm).  $T_4T_2$  was assigned to (16,3) with a diameter of 1.405 nm ( $S_{11} = 1763$  nm,  $S_{22} = 913$  nm,  $S_{33} = 545$  nm,  $S_{44} = 376$  nm).

Previously, it was found that at sufficiently high DOC concentration, all SWCNTs separate in the more hydrophilic DX phase, which was interpreted as the critical concentration for SWCNTs to be coated with a completed DOC layer.<sup>57</sup> For SC, this critical concentration is slightly higher (~0.2 to 0.3%), whereas for SDS-dominated interfaces, the SWCNTs normally separate in the less hydrophilic top phase.<sup>54</sup> Surfactant concentration and competition between the surfactants then determine the ATPE separation. In the competition for the SWCNT surface, at equivalent surfactant concentrations, it is often observed that the binding affinity follows the order DOC

> SC >> SDS, with each of them also depending on the SWCNT  $(n,m)$  type.<sup>56</sup> In the current contribution, global surfactant concentrations of 0.15% DOC/0.225% SDS/0.9% SC were employed. The role of each surfactant is shown in Figure 1b, and a description of how these conditions were obtained is discussed later.

In the past, the importance of DOC to pH-driven ATPE has been discussed by Li et al.,<sup>56</sup> and both DOC and SC have similar chemical structures and might *a priori* be expected to behave similarly. In brief, the protonation of the carboxylic acid on DOC (or SC) leads to its aggregation and the replacement



by SDS on the nanotube's surface. The susceptibility to protonation by acid addition for the two bile salts is similar (DOC,  $pK_a$  6.6; SC,  $pK_a$  6.4) and is much larger than that for SDS.<sup>56,58</sup> Despite their similarity, DGU experiments have demonstrated that for SC, the density of the SWCNT/surfactant complexes shows pronounced variations with SWCNT structure up to large diameters, indicating a much more pronounced variation of surfactant packing than with DOC.<sup>45,59</sup> These variations were moreover shown to be enhanced with decreasing SC concentration (0.7 vs 2%).<sup>45</sup> The marked differences in surfactant coating between SC and DOC were attributed to the extra OH group on the cholesterol moiety of SC, creating a polar face and forcing a face-on stacking on the SWCNT surface, which is more structure- and diameter-selective (leaving gaps in the surfactant coating depending on how the stacking matches the circumference of the tubes and creating large variations in density as well as in hydrophobicity), whereas DOC has only one polar edge, allowing for a more flexible, overlapping stacking on the SWCNT wall, which can hence more flexibly adapt to different diameters.

The strategy for isolating single SWCNT species in the large-diameter range is thus to determine conditions under which a lower  $pK_a$  bile salt surfactant, in this case SC, will continue to cover most SWCNT ( $n,m$ ) species as the DOC content is effectively depleted through the acid addition. This is the basis for enhancing the otherwise insufficient contrast at two separation stages for single ( $n,m$ ) species in the >1.4 nm regime. At the specific surfactant concentrations used, SWCNTs begin in the more hydrophilic DX phase, indicating a complete coating by the bile salt surfactants. By increasing the acid addition, bile salt molecules are preferentially removed from the SWCNT surface, leading to partial coverage by SDS and eventual migration to the top phase. It is expected that those ( $n,m$ ) species with the least complete bile surfactant coating will be the first to become covered by SDS (or at least a disrupted bile salt coverage) and hence the first to migrate into the PEG phase. As previously shown by DGU,<sup>45,59</sup> an incomplete bile-salt stacking around the SWCNT is promoted by the inclusion of SC. Whereas the exact surfactant packing in the DGU work may not be directly comparable to the present conditions, as here a three-surfactant system is used, the specific diameter-dependent stacking of SC on the SWCNT walls does explain why adding SC is required for this separation. Here the structure-dependent surfactant stacking is even further enhanced by the precisely balanced competition with the other surfactants (combination with DOC) and by the extreme sensitivity of the ATPE separation to subtle differences in the surfactant coating. This allows for the resolution of SWCNT ( $n,m$ ) species to the single-enantiomer level.

**Separation and Spectral Analysis.** In this contribution, electric-arc (EA)-discharge-synthesized SWCNTs were used as the starting material. The EA-SWCNTs have open ends, and to avoid water filling, endohedral filling with hexadecane ( $C_{16}H_{34}$ ) was performed prior to separation.<sup>44</sup> EA-SWCNTs have an average diameter of  $\sim 1.55$  nm, with their full diameter distribution spanning approximately 1.25 to 1.7 nm, and have  $S_{11}$  features in the 1550–2100 nm wavelength range,  $S_{22}$  features in the 900–1100 nm range, and  $S_{33}$  features in the visible (450–550 nm) wavelength range.  $M_{11}$  features are centered around  $\sim 650$  nm. To ease separation, all SWCNT samples in this work were first purified of impurities using bulk

centrifugation, followed by rate-zonal ultracentrifugation<sup>60</sup> to remove residual small bundles and other remaining impurities. This parent dispersion was subsequently processed via ATPE<sup>39,55,60</sup> to yield highly separated *s*- and *m*-SWCNT parent populations. Absorbance spectra of the parent  $C_{16}H_{34}@EA$  populations are presented in Figure 1c. As discussed later, additional parent suspensions were also tested, and their absorbance spectra along with PLE maps can be found in the Supporting Information (SI) in Figures S1 and S13. These samples consisted of alternative endohedral fillings ( $H_2O$  or  $C_{24}H_{50}$ ), EA-AP (as-prepared) SWCNTs, which are essentially the same as EA but contain some close-ended (and thus empty) SWCNTs, and two other raw soot sources, known as PT and EA2. EA2 are also electric-arc-discharge SWCNTs but consist of a slightly smaller average ( $n,m$ ) distribution compared with the EA and EA-AP samples. In all cases, the spectra show strong and sharp absorbance features, which are sharpened in comparison with water-filled SWCNTs by the predispersion filling with an alkane.

Absorption spectra for the first six top-phase fractions ( $T_1$ – $T_6$ ) at stage 1 for the semiconducting  $C_{16}H_{34}@EA$  parent are shown in Figure 2a. Spectra for the complete ( $T_1$ – $T_{12}$ ) top-phase fractions are reported in the SI (Figure S2). Excitingly, the first three ( $T_1$ – $T_3$ ) fractions as well as the sixth ( $T_6$ ) contain highly enriched chirality SWCNT populations at stage 1. Because of their similarity,  $T_1$ – $T_3$  were combined to yield  $T_{1-3}$ . Both  $T_{1-3}$  and  $T_6$  were concentrated ( $T_{1-3} = 30$  to  $\sim 8$  mL,  $T_6 = 10$  to  $\sim 1.5$  mL) and transferred to  $D_2O$  while removing all polymers using repeated ultrafiltration. The resulting fractions and their spectra are shown in Figure 2b,c, respectively. After concentration, it can be seen that  $T_{1-3}$  is indeed highly pure and can be assigned to the (14,6) species, which has a diameter of 1.411 nm.<sup>61</sup>  $T_6$  is assigned to (15,5) with a diameter of 1.431 nm.<sup>61</sup> The ability to concentrate fractions and exchange solvents in this way is important because it ensures “clean” spectra and allows for accurate chiral identification and purity analysis. Fractions  $T_4$  and  $T_5$  were taken for stage 2 of the cascade, and the results are shown in Figure 2d,e. The original spectra in  $H_2O$  can be found in Figure S3. The nondiscrete nature of the surfactant shell around any ( $n,m$ ) species leads to some breadth in the extraction conditions, even for a uniform population, and  $T_4$  can be seen to contain residual (14,6) from the obtained population primarily extracted in  $T_1$ – $T_3$  due to this effect. To further purify  $T_4$ , these SWCNTs were isolated at stage 2 by the addition of a mimic bottom phase to increase the available DOC concentration, partitioning all other species to the bottom and allowing the extraction of the residual (14,6) in  $T_4T_1$ . After the complete extraction of (14,6), the bottom phase  $T_4B_1$  was re-extracted to the top phase using the acid-addition methodology to form  $T_4T_2$ , which is found to be a single-chirality population assignable from optical characterization (*vide infra*) as the (16,3) species with a diameter of 1.405 nm.<sup>61</sup> The comparison of  $T_1$ ,  $T_4$ , and  $T_5$  reveals that the relative concentration of (14,6) is at first high in  $T_1$ , is reduced to only contaminant-level fractional concentration by the extraction for fraction  $T_4$ , but then is observed again at high fractional concentration in  $T_5$ . This is an indication that there are two different (14,6) populations that adsorb discriminably different surfactant shells in the  $C_{16}H_{34}@EA$  parent. This second population of the (14,6) species is obtained in the greatest fractional concentration in  $T_5T_2$ .

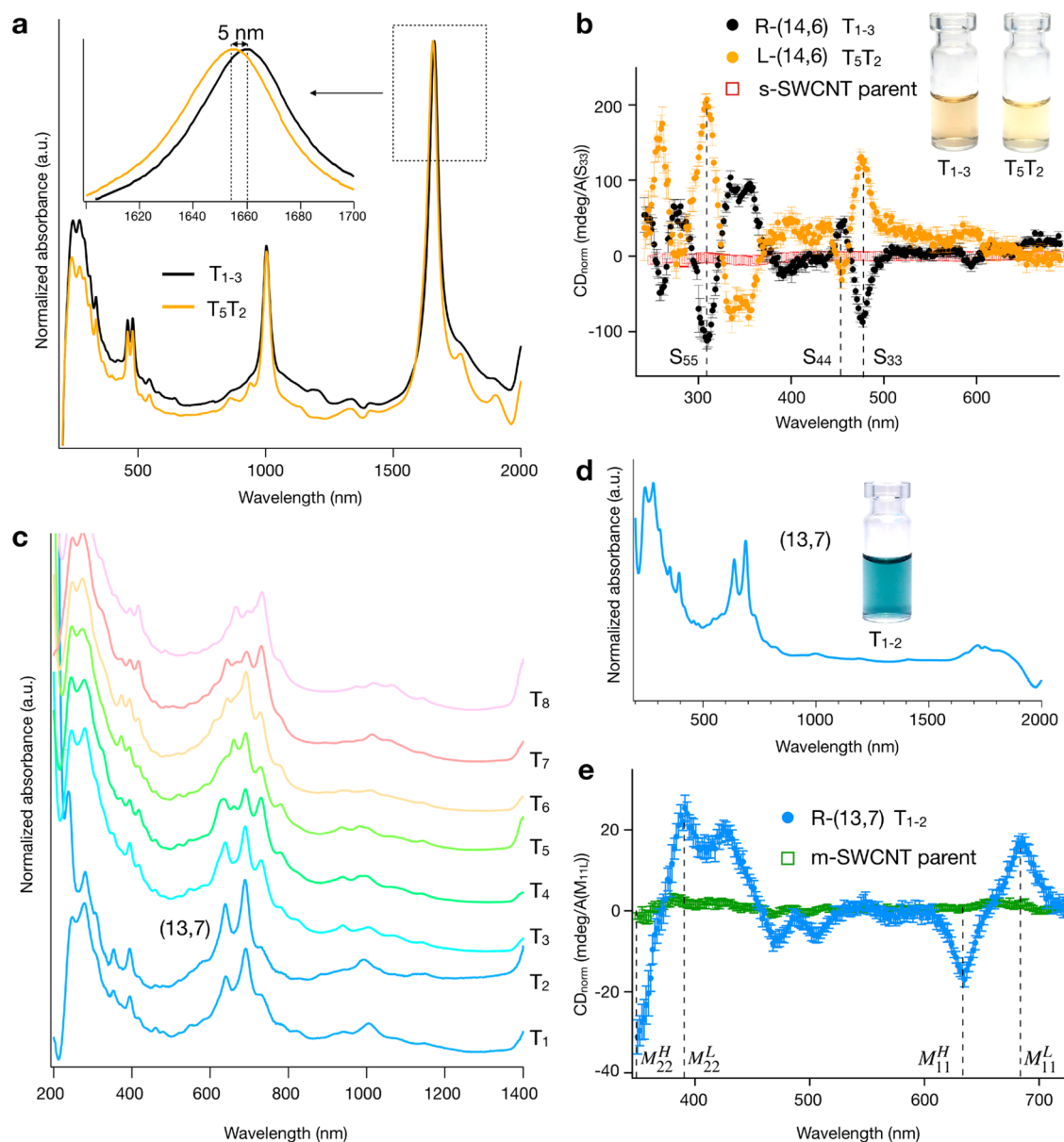


**Figure 3.** Enantiomer enrichment and separation of the C<sub>16</sub>H<sub>34</sub>@EA metallic parent. (a) Absorption in D<sub>2</sub>O and (b) circular dichroism (CD) spectra of the two (14,6) enantiomers (T<sub>1-3</sub> and T<sub>5T2</sub>). CD spectra were referenced against each fraction's S<sub>33</sub> absorption intensity and measured three to seven times in 1% DOC in D<sub>2</sub>O. The error bars represent  $k = 1$  standard deviations of the propagated uncertainties. As scaled by the absorbance of the S<sub>33</sub> peak to correct for the different concentrations of the samples, the two samples have large and near-equal opposing signals at each optical transition (S<sub>33</sub>, S<sub>44</sub>, and higher order). Moreover, the absence of a significant CD<sub>norm</sub> signal from the parent strongly indicates that the two enantiomers are not significantly divergent in abundance in the parent population. (c) Stage-1 separation of the C<sub>16</sub>H<sub>34</sub>@EA metallic parent in H<sub>2</sub>O to obtain a series of top-phase fractions (T<sub>1</sub>–T<sub>8</sub>). The upgoing signal at 1400 nm is due to H<sub>2</sub>O. (d) T<sub>1</sub> and T<sub>2</sub> were combined, concentrated, and transferred to D<sub>2</sub>O to improve the spectral clarity. (e) CD spectrum of (13,7). T<sub>1-2</sub> in panel d is assigned to (13,7) with a diameter of 1.40 nm ( $M_{11}^H = 689$  nm,  $M_{11}^L = 638$  nm), where the presence of two peaks is due to trigonal warping effects.

Following on from the results of Figure 2, a question arises as to whether it is possible to obtain further single-chirality species. Examination of higher order fractions at stage 1 (T<sub>7</sub>–T<sub>12</sub>, Figure S2) were not found to contain single-chirality species, and those fractions that appeared to be ideal candidates for separation at stage 2 (T<sub>7</sub>, T<sub>8</sub>, Figure S3) were unable to be further enriched (T<sub>7-8</sub>, Figure S3c). Nevertheless, a clear trend of increasing diameter can be seen from T<sub>1</sub> to T<sub>12</sub>. The inability to enrich other species implies that for 0.15% DOC/0.225% SDS/0.9% SC, the surfactant shells around (15,5), (16,3), and two populations of (14,6) are very different

compared with all of the other species in the C<sub>16</sub>H<sub>34</sub>@EA parent, which are extracted under conditions consistent with the weaker SDS–DOC diameter dependence previously reported by Fagan et al.<sup>39</sup> This dependence does not generate a sufficient difference in surfactant shells between other species under the current global surfactant conditions to enable resolution in two stages by pH-driven ATPE. This is strongly consistent with the previous DGU experiments and our strategy previously outlined to find a resolving surfactant concentration, as DGU reports only showed a fluctuation in the SC coating around SWCNT species with a diameter close

to (14,6).<sup>45</sup> The importance of the global surfactant concentration being appropriately tailored is highlighted in Figure S4, where the DOC concentration is varied from 0 to 0.2% for a stage-1 separation of (14,6). For the addition of similar aliquots of HCl, the purity of the (14,6) fraction is dramatically reduced on either side of 0.15% DOC and demonstrates the highly sensitive role played by the surfactant concentration in the relative competition with SDS and SC. Furthermore, the importance of SC in combination with DOC is shown in Figure S5, where a comparable separation to that in Figure 2a was not obtained in the absence of SC. The next species in the EA parent with a diameter closest to those isolated in this work is (17,1), but its low abundance makes enrichment and observation difficult. This is followed by (12,8), but it is clear that the isolation of it and other (*n,m*) species will require further optimization of the global surfactant conditions and is the focus of future work.

The most exciting notion about the discriminably different extraction conditions for two (14,6) populations from the same source soot is that these two populations are the left- and right-handed enantiomers, that is, (14,6) and (20, -6), differing in structure only in the twist direction of the carbon lattice. Absorbance spectra of the two (14,6) populations ( $T_{1-3}$ ,  $T_5T_2$ ) are shown in Figure 3a and are consistent with this hypothesis. (See also Figure S23.) The absorbance spectra of the two (14,6) populations are nearly identical, except for a slight red shift of  $T_{1-3}$  relative to  $T_5T_2$  of 5 nm at the  $S_{11}$  ( $\Delta = 2.2$  meV). The shift for  $S_{22}$  (0.5 nm,  $\Delta = 0.5$  meV),  $S_{33}$  (0.6 nm,  $\Delta = 3.2$  meV), and  $S_{44}$  (0.3 nm,  $\Delta = 1.2$  meV) is <1 nm and below the resolution of our instrument. This sort of difference has previously been observed for small-diameter SWCNT enantiomers,<sup>62</sup> for which the different packing structure of the naturally handed surfactant, in our case DOC or SC, on (*n,m*) versus (*n + m*, -*n*) leads to differences in the dielectric environment experienced by the SWCNT. Moreover, as shown in Figure 3a, it is the fraction  $T_{1-3}$  that is red-shifted, which suggestive of a larger dielectric constant, such as would be expected for a CNT surface exposed more to water due to a less complete surfactant coverage (both fractions were dispersed in 1% DOC in D<sub>2</sub>O for the measurement), in line with the weaker adsorption of DOC to the  $T_{1-3}$  (14,6) SWCNT interface and the partition order of  $T_{1-3}$  before  $T_5T_2$ .

Circular dichroism (CD) absorbance spectroscopy is, however, the primary characterization method for determining enantiomer enrichment and handedness of SWCNT populations. CD spectra and photographs of  $T_{1-3}$ ,  $T_5T_2$ , and the parent semiconducting SWCNT dispersion are presented in Figure 3b. CD spectra of the fractions demonstrate the two (14,6) populations to be highly enriched in opposite twist enantiomers ( $T_{1-3} = R\text{-(14,6)}$ ,  $T_5T_2 = L\text{-(14,6)}$ ) and to an approximately equal degree, as scaled by the absorbance of the  $S_{33}$  optical transition to account for concentration differences between the samples.<sup>63</sup> CD spectra of the (15,5) and (16,3) fractions are shown in Figure S12 and also are observed to have strong CD signals. Despite the inability to isolate both enantiomers for each species, highly enantiomer-enriched populations of  $R\text{-(15,5)}$  and  $R\text{-(16,3)}$  were obtained.

Similar separations using the acid-addition ATPE strategy are achievable for metallic SWCNTs, with a stage-1 separation of metallic  $C_{16}H_{34}@EA$  shown in Figure 3c and stage-2 separation shown in Figure S6. Unlike with the semiconducting parent, further enrichment at stage 2 was not

found to yield additional single-chirality species. However, the discrimination of species is significantly more difficult for metallic than semiconducting SWCNTs.<sup>39</sup> Combining and concentrating fractions  $T_1$  and  $T_2$  at stage 1 into 1% DOC in D<sub>2</sub>O (i.e., to form  $T_{1-2}$ ), it can be seen that a single (*n,m*) is highly enriched by the procedure. The absorbance spectra of this fraction are reported in Figure 3d and can be assigned to (13,7) with a diameter of 1.40 nm.<sup>64</sup> Prior to this measurement, it should be noted that contamination from residual semiconducting species (absorbing in the 1600–1800 nm range in  $T_1$  and  $T_2$ ) was removed from  $T_{1-2}$  by performing a second semiconducting/metallic separation. Despite being of a different electronic type, it is worth noting that (13,7) and (14,6) have similar diameters and that they both partition into the upper, PEG-rich ATPE phase after the addition of similar HCl aliquots and thus appear in fractions  $T_1$ – $T_3$ . This implies that for the global surfactant conditions used, it is the nanotube diameter that is primarily determining the surfactant shell and not the electronic type. Other metallic species with similar diameters to the (14,6), (15,5), and (16,3) fractions include the (12,9), (16,4), (17,2), and (18,0) fractions; however, we were unable to isolate these species from the EA population. Except for the (16,4) fraction, this is likely attributable to the lower abundance of those species in the starting material. As shown in Figure 3e, the (13,7) fraction isolated in fraction  $T_{1-2}$  is also enantiomerically enriched, with the population in  $T_{1-2}$  the  $R\text{-(13,7)}$  enantiomer, as determined by the CD spectra.

To demonstrate that the obtained fractions are not an artifact from the use of a certain batch of starting material, we repeated the separation with multiple other SWCNT populations with different filler molecules and from other sources. For all cases, the surfactant concentrations and HCl additions used were comparable to those for the  $C_{16}H_{34}@EA$  samples. For alkane-filled SWCNT populations, highly equivalent separations were generated to those described above; as an example, separation results for a  $C_{24}H_{50}@PT$  semiconducting parent are reported in Figure S7. There are slight variations attributable to the different (*n,m*) distributions of the EA and PT SWCNTs, but the fact that the (14,6) species appears in an identical fraction ( $T_1$ ) supports the hypothesis of the separation dependence upon the surfactant shell composition, which is, in turn, coupled to the nanotube species rather than a process that is specific to a particular raw soot.

Importantly, the second set of control experiments investigated the effects of endohedral filling on the separation, including results on semiconducting separated populations from  $H_2O@EA$ ,  $H_2O@EA2$ , and empty EA-AP-SWCNT parents. Results from these experiments suggest that alkane filling affects the separation more significantly than simply reducing spectral broadness during postseparation characterization. For both semiconducting  $H_2O@SWCNT$  parent populations the purity of the extracted (14,6) and other species was dramatically reduced, and it became difficult to obtain single-chiral species at stage 1 or 2. In both cases, additional SWCNTs ( $S_{11} \approx 1750\text{--}1850$  nm) were found to partition with (14,6), and this was also accompanied by a reduction in yield (concentration) relative to the alkane-filled samples; the spectra of the fraction extracted from the  $H_2O@EA$  SWCNT and  $H_2O@EA2$  semiconducting populations are reported in Figures S8 and S9, respectively. In contrast, for the empty@EA-AP parents (Figures S10 and S11), the separation of (14,6), (16,3), and (15,5) was found to be possible, with the



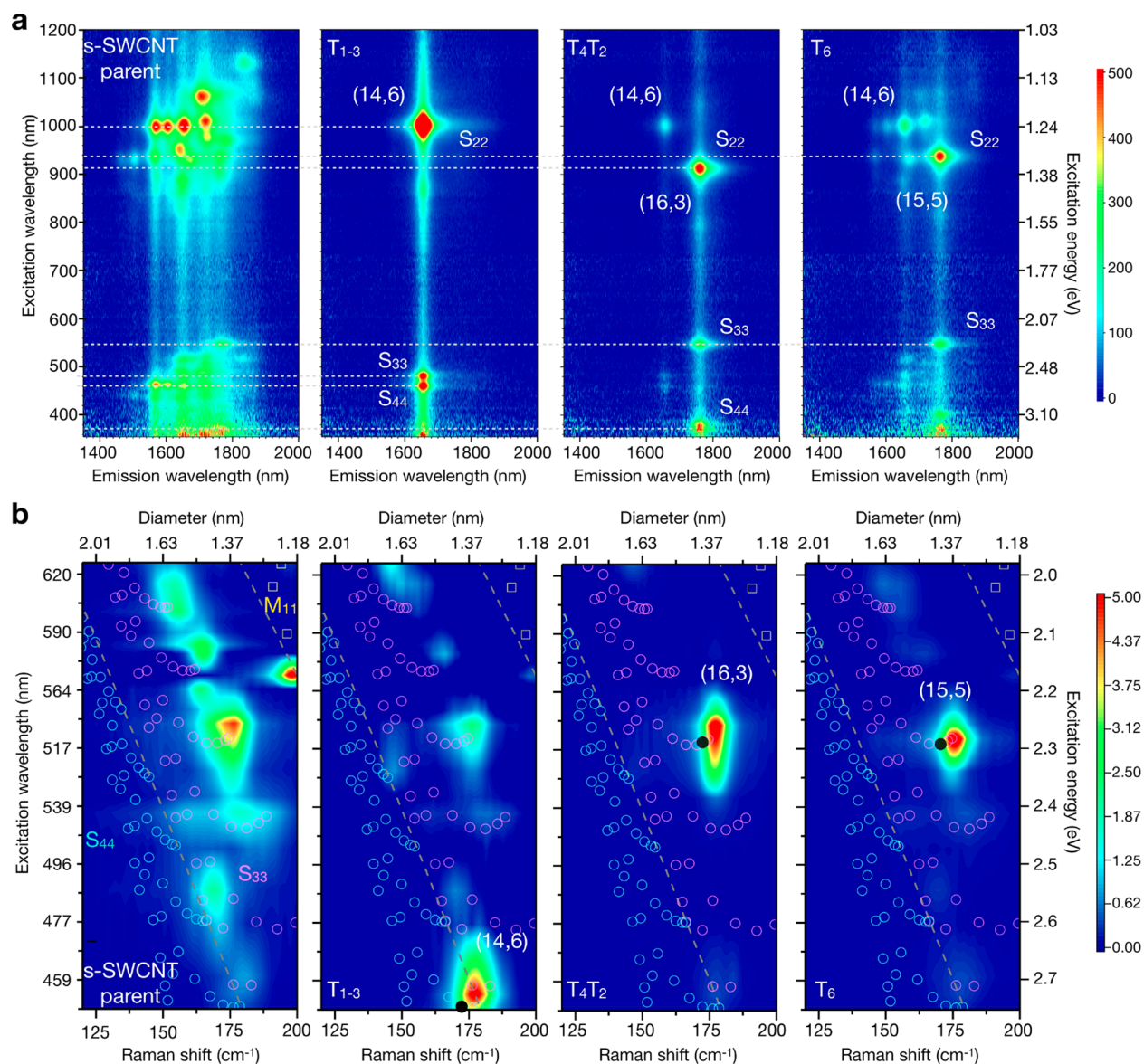


**Figure 4.** Optical characterization of fractions obtained from the semiconducting  $C_{16}H_{34}@EA$  parent. (a) Photoluminescence excitation (PLE) map and (b) radial breathing mode (RBM) resonance Raman maps constructed from spectra at 20 different excitation energies. A dashed line indicates excitation via  $S_{22}$ ,  $S_{33}$ , or  $S_{44}$  in the PLE maps and divides energy ranges where the resonance of  $S_{44}$ ,  $S_{33}$ , and  $M_{11}$  is expected in the Raman maps. The cyan ( $S_{44}$ ) and magenta ( $S_{33}$ ) open circles and yellow ( $M_{11}$ ) open squares are from the Kataura plot and indicate the transition energy as a function of tube diameter. A solid circle indicates the expected Raman shift for the  $(n,m)$  species displayed.

fraction numbers closely following those of the  $C_{16}H_{34}@EA$  parent. The purity and yield were also higher compared with the  $H_2O$ -filled samples. Unfortunately, a similar spectral shoulder to those observed for the water-filled SWCNTs was observed in several of the fractions ( $\sim 1750$ – $1850$  nm in ( $T_3T_1$ ,  $T_2$ )), reducing the achieved purity relative to the  $C_{16}H_{34}$ -filled fractions. This is likely the result of  $<100\%$  isolation of empty SWCNTs from residual water-filled EA-AP-SWCNTs during the rate-zonal centrifugation, the presence of which were confirmed in the population using Raman spectroscopy (Figure S26a). This highlights an additional benefit of using alkane-filled SWCNTs, which is that the population should be entirely alkane-filled and so should not suffer from heterogeneity, as a population of empty SWCNTs contaminated with solvent-filled ones can.

This observation of a significant improvement in ATPE resolution for alkane-filled and empty SWCNTs over water-filled ones may significantly explain why it has taken so long for single-chiral species in the large-diameter regime to appear in the literature. During sonication, to disperse the CNTs with surfactants, any open-ended nanotubes will fill with the solvent, and many closed-ended (i.e., empty) SWCNTs (if there are any in the population to begin with) will break and spontaneously fill with solvent.<sup>60</sup> In their previous report, Fagan et al.<sup>39</sup> utilized almost exclusively empty SWCNTs separated after sonication for their reported SDS-DOC ATPE experiments, but primarily to aid characterization, and so did not draw this conclusion. It is possible to speculate that such endohedral water (and hydronium or oxygen species), and potentially cations, dramatically increases the heterogeneity of the chemical environment felt by the surfactant around the



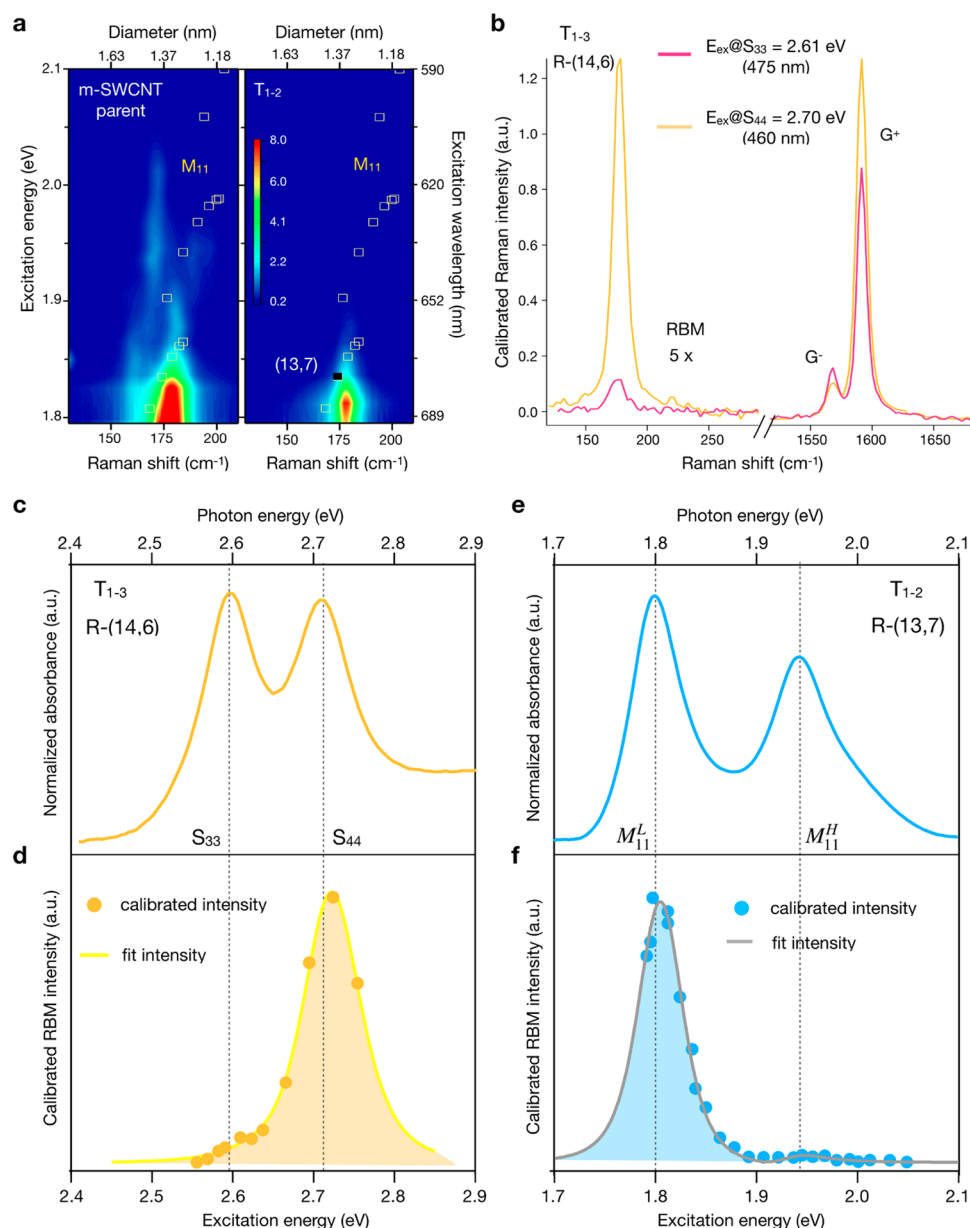


**Figure 5.** Characterization by RBM resonance Raman maps and Raman intensity profile. (a) RBM resonance Raman map of  $C_{16}H_{34}@R-(13,7)$ . The yellow ( $M_{11}$ ) open squares are from the Kataura plot and indicate the transition energy as a function of tube diameter. A solid square indicates the expected Raman shift for (13,7). (b) Comparison of the RBM: $G^+$  intensity for excitation at  $S_{33}$  and  $S_{44}$  of R-(14,6). (c) Absorption spectra of R-(14,6) compared with (d) the calibrated Raman intensity. (e) Absorption spectra of R-(13,7) compared with (f) the calibrated Raman RBM for excitation at  $M_{11}^L$  and  $M_{11}^H$ .

nanotubes. Ideally, the chemical environment for adsorption to the SWCNT sidewall is specified by the intrinsic lattice structure of the nanotube itself, and this translates into a variation in the surfactant coverage between ( $n,m$ ) species and enantiomers. With the inclusion of water, however, it seems apparent that a sufficient proportion of that chemical environment is determined by the effects of water broadening the partition coefficient curves for SWCNTs and greatly reducing discrimination in ATPE. This is one of the key scientific findings of our work and is expected to be relevant not just for ATPE separation but for all surfactant-based methods. To date, the endohedral environment has been neglected (in separation methods not reliant upon density), but here we show that it is a controlling factor for nanotube separation.

Having isolated near-mono chiral and highly enantiomer-enriched populations of the (14,6) and other species, we also utilized the additional optical characterization methods of PLE and resonant Raman spectroscopy (RRS) to quantify the success of the separations and to explore intrinsic optical phenomena.

**Photoluminescence Excitation Spectroscopy.** 2D PLE maps allowed ( $n,m$ ) purity to be quantified in the semi-conducting fractions. Fractions from the  $C_{16}H_{34}@EA$  semi-conducting parent are shown in Figure 4a. Spectra for the  $C_{24}H_{50}$ ,  $H_2O$ -filled, and empty fractions can be found in Figure S14. Histogram plots of the photoluminescence intensity were then generated from advanced fitting of the PLE maps, as outlined in the SI for each sample, and are provided in Figures S15–S22. For the  $C_{16}H_{34}$ -filled samples, the purity of the

separated populations was determined to be 79, 69, 78, and 44% for R-(14,6), L-(14,6), R-(16,3), and R-(15,5), respectively, although ignoring differences in photoluminescence (PL) quantum yield and absorption cross sections. This is compared with total (both enantiomer) fractional concentrations in the parent population of  $\sim 9.2\%$  (including both (14,6) enantiomers), 3.7% for the (16,3), and 4.4% for the (15,5). Applying the method of Yomogida et al.,<sup>23</sup> which takes the ratio of the enantiomer mass to the total mass of the semiconducting parent, we were able to estimate the yield of the enriched fractions to be 8.1, 1.7, 1.5, and 3.8% for the R-(14,6), R-(16,3), L-(14,6), and R-(15,5), respectively. This calculation considers interfacial trapping, which was estimated to be 32% of the semiconducting parent. The purity of  $C_{24}H_{50}$  filled (14,6) from the PT parent was also high at 75%. As expected from the previous discussion, the empty samples were less pure with 71, 59, and 49% for (14,6), (16,3), and (15,5), and the  $H_2O$ -filled samples were below this at 20–40%. As seen previously by Cambré et al.<sup>45,52</sup> and others,<sup>60</sup> the endohedral environment strongly impacts the spectral position of the observed emission. Relative to the empty samples, the endohedral filling red-shifted the  $S_{11}$  emission of (14,6) by  $\sim 30$  nm for  $H_2O$  and  $\sim 14$ –16 nm for the alkanes. A 3 nm shift in the emission wavelength was also observed between the two  $C_{16}H_{34}@ (14,6)$  enantiomers, as shown in Figure S23, consistent with the work of Ghosh et al.<sup>30</sup> and the 5 nm  $S_{11}$  shift previously noted in the absorbance analysis.

**Raman Spectroscopy.** The sorted fractions were additionally characterized with 2D resonant Raman maps, which were constructed from radial breathing mode (RBM) spectra at 20 different excitation energies. These are displayed in Figure 4b for the semiconducting fractions and Figure 5a for the metallic fractions. The raw data can be found in Figures S24a–e and S25a,b. The excitation range partially covered the  $S_{33}$  (blue dots) and  $S_{44}$  (violet dots) transitions, and the chirality assignment data were obtained from Araujo et al.<sup>65</sup> and Doorn et al.<sup>66</sup> In the  $C_{16}H_{34}@EA$  semiconducting parent, multiple intense peaks are present, each composed of signals from multiple chiralities of similar diameters and transition energies. In the enriched samples, only one SWCNT dominates. Figure S24f provides a closer examination of the RBM spectra obtained at 2.75 eV, where the parent and  $T_4T_2$  samples are compared in resonance with  $S_{33}$ . The RBM spectrum of the parent consists of several peaks (gray and red), whereas the spectrum of  $T_4T_2$  has only one belonging to R-(16,3) and is evidence of excellent enrichment. RRS maps are particularly important for the characterization of metallic SWCNT populations because these species are not active in PLE. RRS confirms the isolation of R-(13,7) in its enriched sample, and once again, a comparison of single-line RBM spectra obtained at 1.8 eV for the  $C_{16}H_{34}@EA$  metallic parent and  $T_{1-2}$  in Figure S25c shows a dramatic reduction in the number of peaks. The narrow peak observed in  $T_{1-2}$  is resonant with  $M_{11}^L$  of R-(13,7) and is in contrast with the five different RBMs in the parent.

We also use the characterization of the separated samples with RRS to extract for the first time precise transition energy and RBM shifts due to the alkane filler as compared with empty SWCNTs without the confounding effects of a multispecies population. In Figure 4b, it can be seen that the transition energies differ between the empty SWCNTs (black dots) and the  $C_{16}H_{34}$ -filled samples. By applying third-order perturbation theory to the Raman profile<sup>67</sup> (solid lines in

Figure 5d,f), the transition energies were obtained, and the absolute values are listed for all species in Table S8.  $S_{44}$  of the alkane-filled (14,6) species and  $S_{33}$  of the (15,5) and (16,3) species were found to shift 40 and 10 meV, respectively, to lower energies relative to the empty SWCNTs.

The RBM frequencies of the  $C_{16}H_{34}$ -filled SWCNTs exceeded those of the empty species by 2–8  $cm^{-1}$ . RBM spectra and peak positions for the empty, alkane-, and water-filled SWCNTs can be found in Figure S26. The RBM peak of the empty nanotube fits the expected position,<sup>67</sup> and filling stiffens the radial vibration and alters the RBM frequency. The effects are best observed using the example of the (14,6) species. Once the nanotube is filled with water molecules, the RBM peak of the (14,6) species is shifted to a higher frequency, although this is partially obscured by the reduced purity of the population separable from a water-filled population. A shift of 5  $cm^{-1}$  between empty and water-filled samples is consistent with previous studies.<sup>46,68</sup>  $C_{16}H_{34}$  filling provides an additional upshift of 1  $cm^{-1}$  compared with water-filled species. The absence of two peaks for the alkane-filled sample suggests that it is more homogeneous compared with the water-filled samples. The water-filled sample contains both empty and water-filled nanotubes and a small quantity of other ( $n,m$ ) types, as shown in the absorption data. RBM frequencies of the R and L (14,6) enantiomers in 1% DOC/ $H_2O$  were found to be the same within an experimental error of 0.005  $cm^{-1}$ . All other chiralities were found to have a similar shift between the empty and  $C_{16}H_{34}$ -filled cases. Combined with the transition energy shift, the change in RBM frequency shifts suggests a high packing density of alkane chains inside the nanotube. This is an example of the versatility of the nanotube physics, where optical properties can be tailored by the endohedral filler.

Another characterization made possible by the obtainment of large-diameter SWCNTs is related to exciton–phonon coupling. The transition number and  $(2n + m) \bmod 3$  type of an SWCNT define the position in the reciprocal space where the exciton formation occurs. The exciton–RBM coupling is high for the excitons originating from the K–M valley, whereas in the K– $\Gamma$  valley, it is weak.<sup>69</sup> (14,6) is a type-1 s-SWCNT; therefore,  $S_{33}$  is in the K– $\Gamma$  valley and  $S_{44}$  is in the K–M valley. The RBM intensity profile of (14,6) covering  $S_{33}$  and  $S_{44}$  is shown in Figure 5d. The intensity of the RBM in resonance with  $S_{44}$  was found to be up to 20 times larger compared with the  $S_{33}$ . For comparison, the absorption cross section does not contain a phonon-coupling term and has very similar cross sections for  $S_{33}$  and  $S_{44}$  (Figure 5c). On the contrary, (13,7) is a metallic SWCNT, and the Raman profile shows a significant enhancement at  $M_{11}^L$  and almost no intensity at  $M_{11}^H$  despite both transitions having similar absorption cross sections (Figure 5e,f). The low RBM intensity at  $M_{11}^H$  is related to an exciton from the K– $\Gamma$  valley.<sup>66</sup>

To confirm that the interplay of the RBM intensities is related to the exciton–phonon coupling, it is possible to exclude exciton–photon coupling by comparing the RBM and the G modes. The coupling strength between the exciton and the G-mode phonon in semiconducting SWCNTs is proportional to the energy of the excitonic state.<sup>70</sup> The  $S_{33}$  and  $S_{44}$  transitions of (14,6) have close energies and thus provide similar G-mode intensities, in contrast with the RBMs; see Figure 5b. The G mode comprises two components: the G+ longitudinal (LO) and the G– transverse (TO) at 1591 and 1566  $cm^{-1}$ , respectively. The ratios between the RBM and G+

increase dramatically from 0.01 at  $S_{33}$  to 0.25 at  $S_{44}$ . This is consistent with resonance Raman profiles of RBMs and confirms the effects related to exciton–phonon coupling. The resonance window of the G mode is greater than the distance between these transitions, which allows for an overlap of the G-mode Raman profiles. Because of overlap, the phonons excited simultaneously at the different transitions interfere in a peculiar way; the LO (TO) phonons interfere negatively (positively), providing lower (higher) intensity in resonance with  $S_{33}$  compared with  $S_{44}$ . The monochiral samples in this work allow for a direct comparison between the absorbance and the RBM resonance Raman profile across  $S_{33}$  and  $S_{44}$  and confirm that G phonons interfere with each other when transitions are tight enough. Additionally, the RBM intensity oscillates depending on the transition number and the mod 3 type.

**Separation Mechanism.** Having previously discussed the hypothesized ATPE separation mechanism in detail, we now use the separated fractions to analyze the accuracy of this hypothesis. To test the hypothesis that the DOC coating is reduced on the extracted SWCNTs ( $n,m$ ) species relative to the general EA ( $n,m$ ) population, analytical ultracentrifugation (AUC) experiments were conducted at 10 g/L DOC to obtain the anhydrous density of the SWCNT–DOC complex for the (14,6) SWCNT compared with values for the entire semiconducting alkane-filled population. The value of the *s*-SWCNT parent (gray) is from alkane-filled SWCNTs from the same EA soot reported by Campo et al.<sup>44</sup> Results from the AUC experiments, shown in Figure 6a, find that both the (14,6) ( $T_{1-3}$ ) and (13,7) ( $T_{1-2}$ ) populations exhibit the best estimate anhydrous densities greater than the average for the mixed ( $n,m$ ) alkane-filled population. Because of the lower density of a DOC molecule compared with an alkane-filled SWCNT, and in line with previous analysis,<sup>59</sup> this greater anhydrous density of the (14,6) population implies a lower DOC binding density for the (14,6) than for the other SWCNTs in the EA synthesis ( $n,m$ ) distribution. This result thus supports the mechanism hypothesis supporting the separation strategy enabling the separation of the fractions. Other methods for comparatively determining the quantity of bound surfactants are currently infeasible at the quantities of sample produced to date.<sup>71,72</sup>

**SWCNT-FET Devices.** Lastly, to demonstrate the utility of (14,6) as a functional material, we have fabricated SWCNT transistor devices, as shown in Figure 6b. Here it is important to state that the SWCNTs still contain alkane, and no effort was made to remove the filler for final devices. The transistor channel length ( $L_{CH}$ ) was adapted to the AFM-derived nanotube length distribution to obtain short-channel devices in which nanotubes make direct contact between electrodes. All transistor devices show a uniform p-type conduction with a typical on-state current density of  $\sim 1 \mu\text{A}/\mu\text{m}$  at 0.5 V source-drain bias  $V_{SD}$  and an on/off ratio of up to  $6 \times 10^6$ . Out of the nine measured devices (Figure S27), only one device showed metallic behavior, with an off-state current on the order of 3 to 4  $\mu\text{A}$ . To make the number of bridging nanotubes per device countable by SEM, the nanotube density per contact was deliberately kept low to about 1–5 SWCNTs  $\mu\text{m}^{-1}$  by choosing the dielectrophoretic deposition parameters accordingly. In Figure 6c, the conductance per micrometer channel width ( $W_{CH}$ ) versus the on/off ratio is plotted. The data show that the single-chirality SWCNTs in this diameter range are suitable for fabricating transistors with competitive perform-

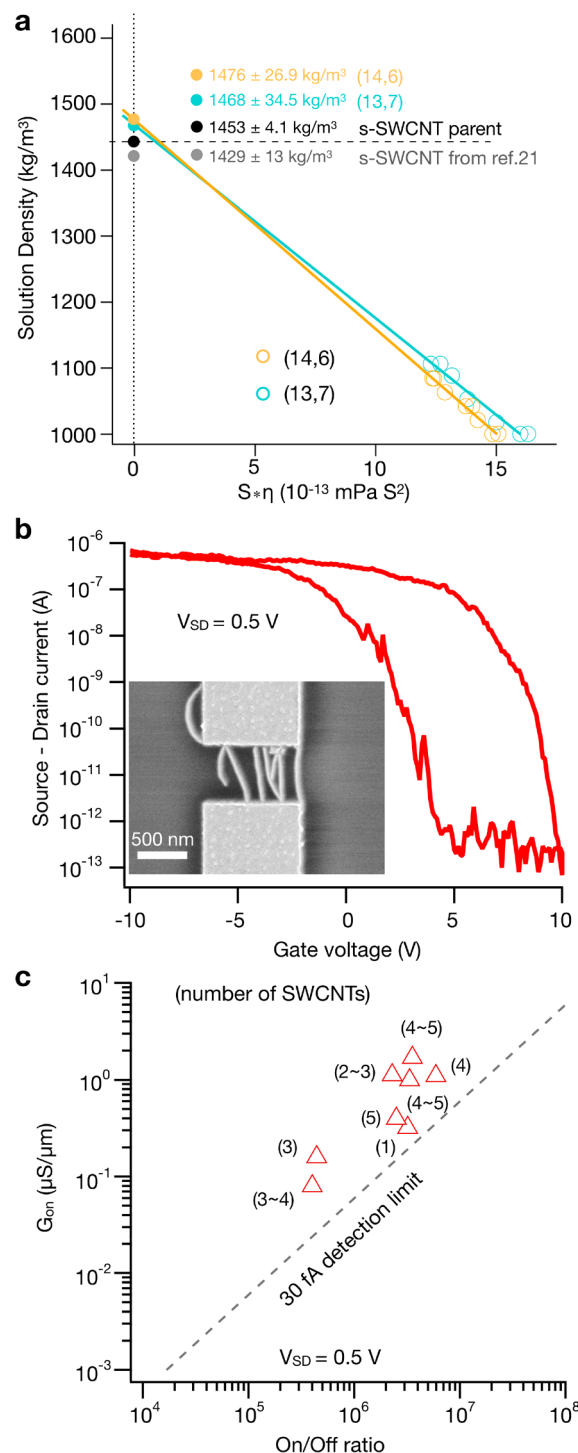


**Figure 6.** Characterization by analytical ultracentrifugation and CNT-FETs. (a) Viscosity-corrected mean sedimentation coefficients for the (14,6) and (13,7) species versus the density of the solution as adjusted by the amount of  $\text{D}_2\text{O}$  (anhydrous density) compared with the *s*-SWCNT parent. Uncertainties are one standard deviation, and experiments were conducted at 10 g/L DOC. (b) Representative curve of the source-drain current versus the gate voltage ( $I_D - V_G I_S$ ) at a source drain voltage ( $V_{SD}$ ) of 0.5 V from the CNT-FET device of  $\text{C}_{16}\text{H}_{34}\text{@R-(14,6)}$ . An SEM image of the device measured is shown as an inset. (c) Scatter plot of the on-state conductance ( $G_{on}$ ) versus the on/off ratio. The number of SWCNTs in a 600 nm channel are indicated between brackets.



ance, in particular, when comparing with transistors made from aqueous solution-processed nanotubes.<sup>73</sup> Still, there is room for improvement. The device mobility,  $\mu$ , as calculated via  $\mu = (L_{\text{CH}}/W_{\text{CH}})(1/C_{\text{G}}V_{\text{SD}})(dI_{\text{SD}}/dV_{\text{G}})$ , with  $C_{\text{G}}$  determined by the parallel plate capacitor model ( $\epsilon_{\text{SiO}_2} = 3.9$ ),<sup>74</sup> is  $10 \pm 5 \text{ cm}^2 \text{ V}^{-1} \text{ s}^{-1}$  and hence is an order of magnitude lower than that in the work of Hennrich et al.<sup>73</sup> This correlates with the order of magnitude lower nanotube density in our devices. By increasing the nanotube density and further shortening the channels, a further increase in the mobility and on-state conductance per nanotube is anticipated. Probing the limits was, however, not the intention of this study (and also screening among tightly packed nanotubes can have detrimental effects on the switching behavior) and is a research subject in itself.<sup>75</sup>

## CONCLUSIONS

Enantiomer-pure fractions of R-(14,6), L-(14,6), R-(16,3), R-(15,5), and R-(13,7) with diameters of  $\sim 1.41 \text{ nm}$  were isolated with a single-chirality purity of up to 80% using a pH-driven ATPE approach. Clear evidence was provided that surfactant-based separations are not limited to small diameters ( $< 1 \text{ nm}$ ), and pH was demonstrated to be a highly sensitive lever for nanotube separation. In the future, it is expected that other surfactant conditions can be found that will soon enable a rich library of other large-diameter species. Here it is predicted that a reduction in the DOC concentration below 0.15% will be necessary, and the use of alkane filling is recommended to improve not only the optical properties but also the homogeneity of the SWCNTs to be separated and thereby the result of the separation. It is expected that monochiral large-diameter SWCNTs will be a valuable tool in the research field of carbon science. Already, in this work, they have allowed for a direct comparison between the absorbance and the RBM resonance Raman profile across  $S_{33}$  and  $S_{44}$  and confirmed that G phonons interfere with each other, and their use in CNT-FET devices appears highly promising.

## METHODS

*Certain equipment, instruments, or materials are identified in this paper in order to adequately specify the experimental details. Such identification does not imply recommendation by the National Institute of Standards and Technology (NIST) nor does it imply the materials are necessarily the best available for the purpose.*

**Materials.** Electric-arc (EA-AP-SWCNT (lot AP-A218) and EA-SWCNT (lot EA-A011) from Carbon Solutions and EA2-SWCNT (lot ASP-100F) Hanwha Chemicals) and plasma-torch (PT-SWCNT, RN220 (lot RNB365) from Raymor Nanotech) SWCNTs were procured from or donated by the manufacturer and utilized without modification. DOC (BioXtra 98+%), SDS (>99%), SC (>99%), and iodixanol (sold as Opti-Prep) were acquired from Sigma-Aldrich and used without further purification. NaClO (10–15% solution) was acquired from Sigma-Aldrich and diluted 1:99 with  $18.1 \text{ M } \Omega \text{ H}_2\text{O}$  to generate a working NaClO stock solution. Poly(ethylene glycol) (PEG,  $M_w$  6 kDa) was acquired from Alfa Aesar. Dextran 70 (DX,  $M_w$  70 kDa) was purchased from TCI. Initial stock solutions of PEG and DX were prepared on a mass/mass basis, and stock surfactant solutions were prepared on a mass/volume basis; iodixanol is sold as a 60% volume fraction stock solution. All solutions prepared from these stock solutions were prepared by volumetric dilution, with nominal

concentrations estimated with respect to the volumetric ratio of the dilution.

**Endohedral Filling.** As previously reported,<sup>44</sup> alkane filling of EA-SWCNT and PT-SWCNT was performed by adding the raw SWCNT powders (160 mg) to  $\sim 10 \text{ mL}$  of hexadecane ( $\text{C}_{16}\text{H}_{34}$ ) or tetracosane ( $\text{C}_{24}\text{H}_{50}$ ) and incubating them for 1 h in the liquid state (at room temperature for  $\text{C}_{16}\text{H}_{34}$  and in an oven at  $60\text{--}65^\circ\text{C}$  for  $\text{C}_{24}\text{H}_{50}$ ). After incubation, the mixtures were filtered (Millipore VVLP membrane,  $0.1 \mu\text{m}$  pore size) at room temperature and washed by heptane to remove the residual alkane on the outside of the SWCNTs. The resulting filter cakes were placed in a fume hood to allow the heptane to evaporate prior to the dispersion with surfactants.

**SWCNT Suspension and Rate-Zonal Centrifugation.** Dispersion and pre-ATPE SWCNT purification have been extensively reported in prior work.<sup>39</sup> In brief, SWCNT powder (1 mg/mL) was dispersed in 2% DOC (20 g/L) solution via tip sonication (45 min, 0.9 W/mL) in an ice bath, followed by centrifugation (Beckman J-2 centrifuge, JA-20 rotor, 1884 rad/s, 2 h), followed by the collection of the supernatant. 8.2 mL aliquots of the supernatant were then layered on top of 28 mL of 10% (volume/volume) iodixanol containing 1% DOC (10 g/L) and ultracentrifuged for 2 h 45 min in a VTi-50 rotor (Beckman-Coulter) at 5240 rad/s (50 000 rpm) at  $20^\circ\text{C}$ . Primary bands in the middle of each centrifuge tube containing well-individualized SWCNTs were collected; for EA-AP SWCNTs, two bands were collected. The top collected band has previously been shown to contain empty, closed-ended SWCNTs, and the lower band contained water-filled SWCNTs.<sup>45</sup> All collected SWCNT populations were concentrated and adjusted toward a 1% DOC (10 g/L) concentration using iterative concentration dilution cycles in a pressurized ultrafiltration stirred cell (Millipore) with either a 100 or 300 kDa molecular weight (MW) cutoff membrane.

**Aqueous Two-Phase Extraction.** The production of the semiconducting and metallic parent populations was performed as previously reported<sup>39,55</sup> and recently extensively described by Fagan.<sup>76</sup> Six parts SWCNT suspension (concentrated in 1% DOC after ultracentrifugation sorting) were mixed with five parts 20% (m/m) DX and four parts 25% (m/m) PEG to perform a first preconcentration (PC) of the SWCNTs and an adjustment of the DOC concentration to  $\sim 0.4\%$ . After discarding the top phase from the PC step, a surfactant adjustment step was performed to further decrease the DOC concentration to  $\sim 0.1\%$  and introduce SC at  $0.9\%$  by adding 1.5 parts 25% (m/m) PEG, 0.8 parts 4.5% SC, and 0.7 parts  $\text{H}_2\text{O}$  to the CNT-containing DX phase (one part). In a second surfactant adjustment step, the DX-rich bottom phase containing almost all SWCNTs (1 part) was mixed with 4.5 parts 25% (m/m) PEG, 1.8 parts 4.5% SC, 1.55 parts 4.5% SDS, and 1.15 parts of  $\text{H}_2\text{O}$  to reach a desired global surfactant concentration of 0.9% SC, 0.7% SDS, and  $< 0.02\%$  DOC. Following the addition of  $6\text{--}10 \mu\text{L/mL}$  NaClO, the metallic species remained in the DX, and the semiconducting species were enriched in the PEG. Iterative isolation was then performed using top (12.5% PEG, 0.9% SC, 0.7% SDS) and bottom (15% DX, 0.9% SC, 0.7% SDS) mimic phases to enrich the metallic and semiconducting fractions. Finally, the metallic nanotubes (one part) in the rich DX phase were pushed to the top PEG-rich phase by adding one part top-phase mimic (12.5% PEG, 1.2% SDS, 0.04% DOC). Metallic and semiconducting populations were concentrated and adjusted toward a DOC concentration of 10 g/L (1%) using iterative

concentration dilution cycles in a pressurized ultrafiltration stirred cell (Millipore) with either a 100 or 300 kDa MW cutoff membrane.

For chiral separation, two parts semiconducting (or metallic) SWCNTs in 1% DOC were mixed with 1 part 20% DX and 1 part 25% PEG to perform an SWCNT PC and adjust the DOC concentration to 0.5%. After discarding the top phase from the PC step, a surfactant adjustment step was performed to further decrease the DOC concentration to  $\sim 0.15\%$  and introduce SC at 0.9% and SDS at 0.225% by adding 1.15 parts 25% (*m/m*) PEG, 0.165 parts 4.5% SDS, 0.66 parts 4.5% SC, and 0.325 parts H<sub>2</sub>O to the CNT-containing DX phase (1 part). After discarding the top phase from the surfactant adjustment step, one part DX-rich bottom phase was iteratively mixed with two parts top mimic phase (12.5% PEG, 0.15% DOC, 0.225% SDS, 0.9% SC), and various HCl additions were made to afford stage-1 separation ( $T_1, T_2, T_3, \dots, T_n$ ). To ensure the accurate extraction of SWCNTs, the suspension near the interface was drawn into a micropipette, and the micropipette was held vertically until the two-phase system separated. The bottom phase was then slowly injected back into the container, leaving only the top phase in the micropipette. With this method, it was possible to obtain at least 95% of the top phase. In the case of large-scale experiments, the suspension near the interface was briefly centrifuged before performing an extraction with a micropipette. The top phases containing single-chirality tubes were used directly for further processing, whereas top phases with multiple (*n,m*) species were added to fresh bottom-phase mimic (15% DX, 0.15% DOC, 0.225% SDS, 0.9% SC) with additional HCl to afford a stage-2 separation ( $T_n T_1, T_n T_2, T_n T_3, \dots, T_n T_m$ ). The exact volumes of the top and bottom phases along with the amount of HCl added at each step can be found in Tables S1–S7. Finally, enantiomer-pure fractions were concentrated and adjusted toward a DOC 1% (10 g/L) concentration in H<sub>2</sub>O or D<sub>2</sub>O using iterative concentration dilution cycles in a pressurized ultrafiltration stirred cell (Millipore) with either a 100 or 300 kDa MW cutoff membrane.

**Absorption and Circular Dichroism Spectroscopy.** UV–vis–NIR absorbance spectra were collected on a Cary 5000 spectrometer from 1880 to 200 nm for samples in H<sub>2</sub>O and from 2500 to 200 nm for samples in D<sub>2</sub>O in 1 nm increments through a 1 or 2 mm quartz cuvette with an integration time of 0.1 s/nm. The spectra of the corresponding blank surfactant solution were collected separately and linearly subtracted during data analysis. CD measurements were performed on an OLIS RSM-090 CD spectrometer with a dual grating monochromator (400 line/nm, 500 nm blaze; two 0.600 mm slits) through a 2 mm path length cuvette in 1.5 nm steps (bandpass  $\sim 2.2$  nm). Multiple measurements were collected for each sample as well as for the matching 10.0 g/L DOC in the D<sub>2</sub>O reference (semiconducting samples) or 10.0 g/L DOC in the H<sub>2</sub>O reference (metallic samples), with reported uncertainties reflecting the total propagated uncertainties including the reference subtraction.

**Photoluminescence Excitation Spectroscopy.** 2D IR PLE spectra were recorded using a home-built setup. The sample was excited with a pulsed Xe lamp (Edinburgh Instruments, Xe900-xP920), and excitation wavelengths were spectrally selected with a 300 mm grating monochromator (Acton SpectraPro 2355). Emission was collected at 90° and analyzed using a 150 mm grating spectrograph (Acton SpectraPro 2156) with a liquid-nitrogen-cooled extended

InGaAs photodiode array detector (Princeton Instruments OMA V:1024/LN-2.2) sensitive up to 2.2  $\mu\text{m}$ . Spectra were recorded with 5 nm steps in excitation wavelength. Appropriate filters were used to eliminate stray light and higher order diffractions from the spectrometers, and all spectra were corrected for detector and spectrograph efficiency, filter transmission, reabsorption within the cell, and (temporal and spectral) variations of the excitation light intensity.

**Raman Spectroscopy.** The Raman spectra were acquired in two experimental setups: The first was optimized for laser excitation energies between 1.9 and 2.2 eV. The light for excitation was produced by a Radiant Dye laser, with Rhodamin 110, R6G, and DCM dyes, and focused on the sample by a lens (N.A. = 0.8). The backscattered light was collected by the same lens and guided into a Horiba t64000 spectrometer with a triple grating configuration. The spectrometer was equipped with 900 grooves per millimeter gratings and a silicon charge-coupled device (CCD). The second setup was optimized for the 2.2 to 2.7 eV excitation range. Light emitted by a Hübner Photonics C-WAVE laser was focused and collected by the same lens (N.A. = 0.8). The Raman light was filtered by a tunable long-pass filter (Semrock) and focused onto the slit of an Andor Kymera 328i spectrometer. The light was dispersed by a 1600 grooves per millimeter grating and analyzed by a silicon CCD. The Raman shift and Raman intensity were calibrated with cyclohexane molecules acquired for each spectrum in the same sample geometry. Raman measurements on the (14,6) samples at 458 nm in Figure S26a were performed using an Ar laser and a Dilor XY800 triple Raman spectrometer.

**Analytical Ultracentrifugation.** AUC was conducted in a Beckman-Coulter XL-I analytical ultracentrifuge with a Ti-50 rotor at 20.0 °C and a rotation rate of 2932 rad/s, similar to previous reports for SWCNT characterization.<sup>77,78</sup> Radial absorbance scans were measured at 245 (data for anhydrous densities) or 460 nm (data for buoyant densities). Prior to starting an experiment, cells were equilibrated for a minimum time of 1.5 h in the instrument to ensure temperature equilibration. The density and viscosity of the exact 10.0 g/L DOC in unenriched water, in 100% (nominal) D<sub>2</sub>O, and in 80% D<sub>2</sub><sup>18</sup>O/20% D<sub>2</sub>O used for the dilution of samples in the experiments were measured separately in an Anton-Parr DMA 5000–LOVIS M densitometer–viscometer. Linear interpolation was used for intermediate isotope concentrations. Typical sample and reference volumes were 400  $\mu\text{L}$  but were reduced to between 300 and 360  $\mu\text{L}$  for D<sub>2</sub><sup>18</sup>O-containing samples. Constant dilution factors were utilized to achieve as similar as possible initial SWCNT concentrations in the measured samples.

The analysis of recorded radial absorbance profiles was conducted using the numerical fitting software SEDFIT.<sup>79,80</sup> Sedimentation was modeled using the *c(s)* model with the measured solution parameters, a discretization to 1/10th of a *s* value, and a regularization of 0.95. The meniscus and noise were fit for each experiment but agreed well with the apparent positions in the data. The initial values for the partial specific volume were taken from previous reports, but the final data evaluation was conducted with values extracted from the extrapolation of the SWCNT sample densities in this contribution. Friction factor values for the (14,6) and (13,7) populations were fit separately and found to be essentially

invariant, as expected, for each population with respect to the isotopic composition of the water.

**SWCNT-FET Fabrication.** Transistor devices were fabricated by the dielectrophoretic deposition of nanotubes onto 45 nm Pd/5 nm Cr thick electrodes, forming 600 nm long and 1  $\mu\text{m}$  wide channels defined by e-beam patterning on a 300 nm  $\text{SiO}_2/p\text{-Si}$  substrate. The SWCNTs were deposited from aqueous dispersion via alternating-current (AC) dielectrophoresis (DEP), as described in previous work.<sup>81</sup> During the DEP process, a drop of 10  $\mu\text{L}$  of diluted dispersion (dilution ratio 1:100) was placed onto the sample, and an AC voltage of 2  $V_{\text{pp}}$  at 300 kHz was applied between the common drain electrode and the  $p\text{-Si}$  back gate. After 5 min, the surface of the sample was repeatedly rinsed with deionized  $\text{H}_2\text{O}$  before the AC field was switched off. All devices were subsequently annealed on a hot plate at 150  $^\circ\text{C}$  in air for 0.5 h. Electrical characterization was conducted in an ambient atmosphere using an Agilent 4155C semiconductor parameter analyzer. Transfer characteristics were measured with back-gate voltage sweeps from  $V_{\text{G}} = -10$  to  $+10$  V (step size 100 mV) at source-drain voltages of 0.5 and 1 V. SEM images were obtained after the electrical characterization with a Zeiss Ultra Plus scanning electron microscope under a 1 kV electron beam.

## ASSOCIATED CONTENT

### Supporting Information

The Supporting Information is available free of charge at <https://pubs.acs.org/doi/10.1021/acsnano.9b08244>.

Additional information on the surfactant conditions required for separation, a comparison of different raw materials and fillers, and further optical and electronic characterization (PDF)

## AUTHOR INFORMATION

### Corresponding Authors

\*E-mail: [han.li@kit.edu](mailto:han.li@kit.edu) (H.L.).

\*E-mail: [jeffrey.fagan@nist.gov](mailto:jeffrey.fagan@nist.gov) (J.A.F.).

\*E-mail: [benjamin.flavel@kit.edu](mailto:benjamin.flavel@kit.edu) (B.S.F.).

### ORCID

Sofie Cambré: 0000-0001-7471-7678

Ming Zheng: 0000-0002-8058-1348

Jeffrey A. Fagan: 0000-0003-1483-5554

Benjamin S. Flavel: 0000-0002-8213-8673

### Author Contributions

H.L., M.Z., J.A.F., and B.S.F. conceived the idea for this work and designed and performed the experiments. G.G., O.G., and S.R. characterized the samples with Raman spectroscopy, and S.C. and W.W. characterized the samples with 2D PLE mapping. N.A.P., P.B.S., S.D., and R.K. performed the electrical characterization with CNT-FETs. All authors analyzed the results and contributed to the preparation of the manuscript.

### Notes

The authors declare no competing financial interest.

## ACKNOWLEDGMENTS

B.S.F. acknowledges support from the Deutsche Forschungsgemeinschaft (DFG) under grant numbers FL 834/2-1, FL 834/2-2, FL 834/5-1, and FL 834/7-1. S.C. and W.W. acknowledge funding from the Fund for Scientific Research Flanders (FWO project nos. G040011N, G02112N, G035918N, and G036618N and the EOS-charming project

G0F6218N [EOS-ID 30467715]) and the European Research Council Starting Grant no. 679841. R.K. acknowledges funding by the Volkswagen Foundation.

## REFERENCES

- (1) Avouris, P.; Chen, Z.; Perebeinos, V. Carbon-Based Electronics. In *Nanoscience and Technology: A Collection of Reviews from Nature Journals*; Rogers, P.; Nature Publishing Group: London, 2009; pp 174–184.
- (2) Arnold, M. S.; Blackburn, J. L.; Crochet, J. J.; Doorn, S. K.; Duque, J. G.; Mohite, A.; Telg, H. Recent Developments in the Photophysics of Single-Walled Carbon Nanotubes for Their Use as Active and Passive Material Elements in Thin Film Photovoltaics. *Phys. Chem. Chem. Phys.* **2013**, *15*, 14896–14918.
- (3) Angione, M. D.; Pilolli, R.; Cotrone, S.; Magliulo, M.; Mallardi, A.; Palazzo, G.; Sabbatini, L.; Fine, D.; Dodabalapur, A.; Cioffi, N.; et al. Carbon Based Materials for Electronic Bio-Sensing. *Mater. Today* **2011**, *14*, 424–433.
- (4) He, X.; Htoon, H.; Doorn, S. K.; Pernice, W. H.; Pyatkov, F.; Krupke, R.; Jeantet, A.; Chassagneux, Y.; Voisin, C. Carbon Nanotubes as Emerging Quantum-Light Sources. *Nat. Mater.* **2018**, *17*, 663–670.
- (5) Rao, R.; Pint, C. L.; Islam, A. E.; Weatherup, R. S.; Hofmann, S.; Meshot, E. R.; Wu, F. Q.; Zhou, C. W.; Dee, N.; Amama, P. B.; Carpena-Nunez, J.; Shi, W. B.; Plata, D. L.; Penev, E. S.; Jakobson, B. I.; Balbuena, P. B.; Bichara, C.; Futaba, D. N.; Noda, S.; Shin, H. M.; et al. Carbon Nanotubes and Related Nanomaterials: Critical Advances and Challenges for Synthesis Toward Mainstream Commercial Applications. *ACS Nano* **2018**, *12*, 11756–11784.
- (6) Zheng, M. Sorting Carbon Nanotubes. *Top. Curr. Chem.* **2017**, *375*, 13.
- (7) Moore, K. E.; Tune, D. D.; Flavel, B. S. Double-Walled Carbon Nanotube Processing. *Adv. Mater.* **2015**, *27*, 3105–3137.
- (8) Arnold, M. S.; Stupp, S. I.; Hersam, M. C. Enrichment of Single-Walled Carbon Nanotubes by Diameter in Density Gradients. *Nano Lett.* **2005**, *5*, 713–718.
- (9) Huang, X.; McLean, R. S.; Zheng, M. High-Resolution Length Sorting and Purification of DNA-Wrapped Carbon Nanotubes by Size-Exclusion Chromatography. *Anal. Chem.* **2005**, *77*, 6225–6228.
- (10) Moore, K. E.; Pfohl, M.; Hennrich, F.; Chakradhanula, V. S. K.; Kuebel, C.; Kappes, M. M.; Shapter, J. G.; Krupke, R.; Flavel, B. S. Separation of Double-Walled Carbon Nanotubes by Size Exclusion Column Chromatography. *ACS Nano* **2014**, *8*, 6756–6764.
- (11) Moore, K. E.; Pfohl, M.; Tune, D. D.; Hennrich, F.; Dehm, S.; Chakradhanula, V. S. K.; Kubel, C.; Krupke, R.; Flavel, B. S. Sorting of Double-Walled Carbon Nanotubes According to Their Outer Wall Electronic Type via a Gel Permeation Method. *ACS Nano* **2015**, *9*, 3849–3857.
- (12) Arnold, M. S.; Green, A. A.; Hulvat, J. F.; Stupp, S. I.; Hersam, M. C. Sorting Carbon Nanotubes by Electronic Structure Using Density Differentiation. *Nat. Nanotechnol.* **2006**, *1*, 60–65.
- (13) Zheng, M.; Jagota, A.; Strano, M. S.; Santos, A. P.; Barone, P.; Chou, S. G.; Diner, B. A.; Dresselhaus, M. S.; Mclean, R. S.; Onoa, G. B. Structure-Based Carbon Nanotube Sorting by Sequence-Dependent DNA Assembly. *Science* **2003**, *302*, 1545–1548.
- (14) Yang, F.; Wang, X.; Zhang, D. Q.; Yang, J.; Luo, D.; Xu, Z. W.; Wei, J. K.; Wang, J. Q.; Xu, Z.; Peng, F.; Li, X. M.; Li, R. M.; Li, Y. L.; Li, M. H.; Bai, X. D.; Ding, F.; Li, Y. Chirality-Specific Growth of Single-Walled Carbon Nanotubes on Solid Alloy Catalysts. *Nature* **2014**, *510*, 522–524.
- (15) Zhang, S. C.; Kang, L. X.; Wang, X.; Tong, L. M.; Yang, L. W.; Wang, Z. Q.; Qi, K.; Deng, S. B.; Li, Q. W.; Bai, X. D.; Ding, F.; Zhang, J. Arrays of Horizontal Carbon Nanotubes of Controlled Chirality Grown Using Designed Catalysts. *Nature* **2017**, *543*, 234–238.
- (16) Nish, A.; Hwang, J.-Y.; Doig, J.; Nicholas, R. J. Highly Selective Dispersion of Single-Walled Carbon Nanotubes Using Aromatic Polymers. *Nat. Nanotechnol.* **2007**, *2*, 640–646.



- (17) Graf, A.; Zakharko, Y.; Schiessl, S. P.; Backes, C.; Pfohl, M.; Flavel, B. S.; Zaumseil, J. Large Scale, Selective Dispersion of Long Single-Walled Carbon Nanotubes with High Photoluminescence Quantum Yield by Shear Force Mixing. *Carbon* **2016**, *105*, 593–599.
- (18) Hwang, J. Y.; Nish, A.; Doig, J.; Douven, S.; Chen, C. W.; Chen, L. C.; Nicholas, R. J. Polymer Structure and Solvent Effects on the Selective Dispersion of Single-Walled Carbon Nanotubes. *J. Am. Chem. Soc.* **2008**, *130*, 3543–3553.
- (19) Shea, M. J.; Mehlenbacher, R. D.; Zanni, M. T.; Arnold, M. S. Experimental Measurement of the Binding Configuration and Coverage of Chirality-Sorting Polyfluorenes on Carbon Nanotubes. *J. Phys. Chem. Lett.* **2014**, *5*, 3742–3749.
- (20) Flavel, B. S.; Moore, K. E.; Pfohl, M.; Kappes, M. M.; Hennrich, F. Separation of Single-Walled Carbon Nanotubes with a Gel Permeation Chromatography System. *ACS Nano* **2014**, *8*, 1817–1826.
- (21) Liu, H.; Nishide, D.; Tanaka, T.; Kataura, H. Large-Scale Single-Chirality Separation of Single-Wall Carbon Nanotubes by Simple Gel Chromatography. *Nat. Commun.* **2011**, *2*, 309.
- (22) Zeng, X.; Yang, D.; Liu, H.; Zhou, N.; Wang, Y.; Zhou, W.; Xie, S.; Kataura, H. Detecting and Tuning the Interactions Between Surfactants and Carbon Nanotubes for Their High-Efficiency Structure Separation. *Adv. Mater. Interfaces* **2018**, *5*, 1700727.
- (23) Yomogida, Y.; Tanaka, T.; Zhang, M.; Yudasaka, M.; Wei, X.; Kataura, H. Industrial-Scale Separation of High-Purity Single-Chirality Single-Wall Carbon Nanotubes for Biological Imaging. *Nat. Commun.* **2016**, *7*, 12056.
- (24) Liu, H.; Feng, Y.; Tanaka, T.; Urabe, Y.; Kataura, H. Diameter-Selective Metal/Semiconductor Separation of Single-Wall Carbon Nanotubes by Agarose Gel. *J. Phys. Chem. C* **2010**, *114*, 9270–9276.
- (25) Flavel, B. S.; Kappes, M. M.; Krupke, R.; Hennrich, F. Separation of Single-Walled Carbon Nanotubes by 1-Dodecanol-Mediated Size-Exclusion Chromatography. *ACS Nano* **2013**, *7*, 3557–3564.
- (26) Jain, R. M.; Ben-Naim, M.; Landry, M. P.; Strano, M. S. Competitive Binding in Mixed Surfactant Systems for Single-Walled Carbon Nanotube Separation. *J. Phys. Chem. C* **2015**, *119*, 22737–22745.
- (27) Tyler, T. P.; Shastry, T. A.; Leever, B. J.; Hersam, M. C. Narrow Diameter Distributions of Metallic Arc Discharge Single-Walled Carbon Nanotubes via Dual-Iteration Density Gradient Ultracentrifugation. *Adv. Mater.* **2012**, *24*, 4765–4768.
- (28) Bonaccorso, F.; Hasan, T.; Tan, P. H.; Sciascia, C.; Privitera, G.; Di Marco, G.; Gucciardi, P. G.; Ferrari, A. C. Density Gradient Ultracentrifugation of Nanotubes: Interplay of Bundling and Surfactants Encapsulation. *J. Phys. Chem. C* **2010**, *114*, 17267–17285.
- (29) Seo, J. W. T.; Yoder, N. L.; Shastry, T. A.; Humes, J. J.; Johns, J. E.; Green, A. A.; Hersam, M. C. Diameter Refinement of Semiconducting Arc Discharge Single-Walled Carbon Nanotubes via Density Gradient Ultracentrifugation. *J. Phys. Chem. Lett.* **2013**, *4*, 2805–2810.
- (30) Ghosh, S.; Bachilo, S. M.; Weisman, R. B. Advanced Sorting of Single-Walled Carbon Nanotubes by Nonlinear Density-Gradient Ultracentrifugation. *Nat. Nanotechnol.* **2010**, *5*, 443–450.
- (31) Khripin, C. Y.; Fagan, J. A.; Zheng, M. Spontaneous Partition of Carbon Nanotubes in Polymer-Modified Aqueous Phases. *J. Am. Chem. Soc.* **2013**, *135*, 6822–6825.
- (32) Turek, E.; Wasiak, T.; Stando, G.; Janas, D. Probing the Mechanics of Aqueous Two-Phase Extraction Using Large Diameter Single-Walled Carbon Nanotubes. *Nanotechnology* **2018**, *29*, 405704.
- (33) Omachi, H.; Komuro, T.; Matsumoto, K.; Nakajima, M.; Watanabe, H.; Hirotani, J.; Ohno, Y.; Shinohara, H. Aqueous Two-Phase Extraction of Semiconducting Single-Wall Carbon Nanotubes with Isomaltodextrin and Thin-Film Transistor Applications. *Appl. Phys. Express* **2019**, *12*, 097003.
- (34) Wei, X.; Tanaka, T.; Hirakawa, T.; Yomogida, Y.; Kataura, H. Determination of Enantiomeric Purity of Single-Wall Carbon Nanotubes Using Flavin Mononucleotide. *J. Am. Chem. Soc.* **2017**, *139*, 16068–16071.
- (35) Peng, X.; Komatsu, N.; Bhattacharya, S.; Shimawaki, T.; Aonuma, S.; Kimura, T.; Osuka, A. Optically Active Single-Walled Carbon Nanotubes. *Nat. Nanotechnol.* **2007**, *2*, 361–365.
- (36) Green, A. A.; Duch, M. C.; Hersam, M. C. Isolation of Single-Walled Carbon Nanotube Enantiomers by Density Differentiation. *Nano Res.* **2009**, *2*, 69–77.
- (37) Akazaki, K.; Toshimitsu, F.; Ozawa, H.; Fujigaya, T.; Nakashima, N. Recognition and One-Pot Extraction of Right- and Left-Handed Semiconducting Single-Walled Carbon Nanotube Enantiomers Using Fluorene-Binaphthol Chiral Copolymers. *J. Am. Chem. Soc.* **2012**, *134*, 12700–12707.
- (38) Liu, H.; Tanaka, T.; Kataura, H. Optical Isomer Separation of Single-Chirality Carbon Nanotubes Using Gel Column Chromatography. *Nano Lett.* **2014**, *14*, 6237–6243.
- (39) Fagan, J. A.; H  roz, E. H.; Ihly, R.; Gui, H.; Blackburn, J. L.; Simpson, J. R.; Lam, S.; Hight Walker, A. R.; Doorn, S. K.; Zheng, M. Isolation of > 1 nm Diameter Single-Wall Carbon Nanotube Species Using Aqueous Two-Phase Extraction. *ACS Nano* **2015**, *9*, 5377–5390.
- (40) Liu, K.; Deslippe, J.; Xiao, F.; Capaz, R. B.; Hong, X.; Aloni, S.; Zettl, A.; Wang, W.; Bai, X.; Louie, S. G.; et al. An Atlas of Carbon Nanotube Optical Transitions. *Nat. Nanotechnol.* **2012**, *7*, 325–329.
- (41) van Bezouw, S.; Arias, D. H.; Ihly, R.; Cambre, S.; Ferguson, A. J.; Campo, J.; Johnson, J. C.; Defiliet, J.; Wenseleers, W.; Blackburn, J. L. Diameter-Dependent Optical Absorption and Excitation Energy Transfer from Encapsulated Dye Molecules Toward Single-Walled Carbon Nanotubes. *ACS Nano* **2018**, *12*, 6881–6894.
- (42) Fagan, J. A.; Khripin, C. Y.; Silvera Batista, C. A.; Simpson, J. R.; H  roz, E. H.; Hight Walker, A. R.; Zheng, M. Isolation of Specific Small-Diameter Single-Wall Carbon Nanotube Species via Aqueous Two-Phase Extraction. *Adv. Mater.* **2014**, *26*, 2800–2804.
- (43) Wenseleers, W.; Vlasov, I. I.; Goovaerts, E.; Obraztsova, E. D.; Lobach, A. S.; Bouwen, A. Efficient Isolation and Solubilization of Pristine Single-Walled Nanotubes in Bile Salt Micelles. *Adv. Funct. Mater.* **2004**, *14*, 1105–1112.
- (44) Campo, J.; Piao, Y.; Lam, S.; Stafford, C. M.; Streit, J. K.; Simpson, J. R.; Hight Walker, A. R.; Fagan, J. A. Enhancing Single-Wall Carbon Nanotube Properties Through Controlled Endohedral Filling. *Nanoscale Horiz* **2016**, *1*, 317–324.
- (45) Cambre, S.; Wenseleers, W. Separation and Diameter-Sorting of Empty (End-Capped) and Water-Filled (Open) Carbon Nanotubes by Density Gradient Ultracentrifugation. *Angew. Chem., Int. Ed.* **2011**, *50*, 2764–2768.
- (46) Wenseleers, W.; Cambre, S.; Culin, J.; Bouwen, A.; Goovaerts, E. Effect of Water Filling on the Electronic and Vibrational Resonances of Carbon Nanotubes: Characterizing Tube Opening by Raman Spectroscopy. *Adv. Mater.* **2007**, *19*, 2274–2278.
- (47) Chen, Z. H.; Appenzeller, J.; Knoch, J.; Lin, Y. M.; Avouris, P. The Role of Metal-Nanotube Contact in the Performance of Carbon Nanotube Field-Effect Transistors. *Nano Lett.* **2005**, *5*, 1497–1502.
- (48) Tune, D. D.; Flavel, B. S. Advances in Carbon Nanotube-Silicon Heterojunction Solar Cells. *Adv. Energy Mater.* **2018**, *8*, 1703241.
- (49) Ihly, R.; Mistry, K. S.; Ferguson, A. J.; Clikeman, T. T.; Larson, B. W.; Reid, O.; Boltalina, O. V.; Strauss, S. H.; Rumbles, G.; Blackburn, J. L. Tuning the Driving Force for Exciton Dissociation in Single-Walled Carbon Nanotube Heterojunctions. *Nat. Chem.* **2016**, *8*, 603–609.
- (50) Piao, Y.; Meany, B.; Powell, L. R.; Valley, N.; Kwon, H.; Schatz, G. C.; Wang, Y. Brightening of Carbon Nanotube Photoluminescence Through the Incorporation of sp<sup>3</sup> Defects. *Nat. Chem.* **2013**, *5*, 840–845.
- (51) Gauffr  s, E.; Tang, N.-W.; Lapointe, F.; Cabana, J.; Nadon, M.-A.; Cottenye, N.; Raymond, F.; Szkopek, T.; Martel, R. Giant Raman Scattering from J-Aggregated Dyes Inside Carbon Nanotubes for Multispectral Imaging. *Nat. Photonics* **2014**, *8*, 72–78.
- (52) Cambr  s, S.; Campo, J.; Beirnaert, C.; Verlackt, C.; Cool, P.; Wenseleers, W. Asymmetric Dyes Align Inside Carbon Nanotubes to

Yield a Large Nonlinear Optical Response. *Nat. Nanotechnol.* **2015**, *10*, 248–252.

(53) Albertsson, P. A. K. *Partition of Cell Particles and Macromolecules*; Wiley-Interscience: New York, 1971.

(54) Subbaiyan, N. K.; Cambré, S.; Parra-Vasquez, A. N. G.; Hároz, E. H.; Doorn, S. K.; Duque, J. G. Role of Surfactants and Salt in Aqueous Two-Phase Separation of Carbon Nanotubes Toward Simple Chirality Isolation. *ACS Nano* **2014**, *8*, 1619–1628.

(55) Gui, H.; Streit, J. K.; Fagan, J. A.; Hight Walker, A. R.; Zhou, C.; Zheng, M. Redox Sorting of Carbon Nanotubes. *Nano Lett.* **2015**, *15*, 1642–1646.

(56) Li, H.; Gordeev, G.; Garrity, O.; Reich, S.; Flavel, B. S. Separation of Small-Diameter Single-Walled Carbon Nanotubes in One to Three Steps with Aqueous Two-Phase Extraction. *ACS Nano* **2019**, *13*, 2567–2578.

(57) Subbaiyan, N. K.; Parra-Vasquez, A. N. G.; Cambré, S.; Cordoba, M. A. S.; Yalcin, S. E.; Hamilton, C. E.; Mack, N. H.; Blackburn, J. L.; Doorn, S. K.; Duque, J. G. Bench-Top Aqueous Two-Phase Extraction of Isolated Individual Single-Walled Carbon Nanotubes. *Nano Res.* **2015**, *8*, 1755–1769.

(58) Sorensen, H.; Sorensen, S.; Bjerregaard, C.; Michaelsen, S. *Chromatography and Capillary Electrophoresis in Food Analysis*; Royal Society of Chemistry: Cambridge, U.K., 2007.

(59) Cambré, S.; Muyshondt, P.; Federicci, R.; Wenseleers, W. Chirality-Dependent Densities of Carbon Nanotubes by *In Situ* 2D Fluorescence-Excitation and Raman Characterisation in a Density Gradient After Ultracentrifugation. *Nanoscale* **2015**, *7*, 20015–20024.

(60) Fagan, J. A.; Huh, J. Y.; Simpson, J. R.; Blackburn, J. L.; Holt, J. M.; Larsen, B. A.; Walker, A. R. H. Separation of Empty and Water-Filled Single-Wall Carbon Nanotubes. *ACS Nano* **2011**, *5*, 3943–3953.

(61) Weisman, R. B.; Bachilo, S. M. Dependence of Optical Transition Energies on Structure for Single-Walled Carbon Nanotubes in Aqueous Suspension: An Empirical Kataura Plot. *Nano Lett.* **2003**, *3*, 1235–1238.

(62) Ao, G.; Streit, J. K.; Fagan, J. A.; Zheng, M. Differentiating Left- and Right-Handed Carbon Nanotubes by DNA. *J. Am. Chem. Soc.* **2016**, *138*, 16677–16685.

(63) Sato, N.; Tatsumi, Y.; Saito, R. Circular Dichroism of Single-Wall Carbon Nanotubes. *Phys. Rev. B: Condens. Matter Mater. Phys.* **2017**, *95*, 155436.

(64) Hároz, E. H.; Duque, J. G.; Tu, X.; Zheng, M.; Hight Walker, A. R.; Hauge, R. H.; Doorn, S. K.; Kono, J. Fundamental Optical Processes in Armchair Carbon Nanotubes. *Nanoscale* **2013**, *5*, 1411–1439.

(65) Araujo, P. T.; Jorio, A.; Dresselhaus, M. S.; Sato, K.; Saito, R. Diameter Dependence of the Dielectric Constant for the Excitonic Transition Energy of Single-Wall Carbon Nanotubes. *Phys. Rev. Lett.* **2009**, *103*, 146802.

(66) Doorn, S. K.; Araujo, P. T.; Hata, K.; Jorio, A. Excitons and Exciton-Phonon Coupling in Metallic Single-Walled Carbon Nanotubes: Resonance Raman Spectroscopy. *Phys. Rev. B: Condens. Matter Mater. Phys.* **2008**, *78*, 165408.

(67) Maultzsch, J.; Telg, H.; Reich, S.; Thomsen, C. Radial Breathing Mode of Single-Walled Carbon Nanotubes: Optical Transition Energies and Chiral-Index Assignment. *Phys. Rev. B: Condens. Matter Mater. Phys.* **2005**, *72*, 205438.

(68) Cambré, S.; Schoeters, B.; Luyckx, S.; Goovaerts, E.; Wenseleers, W. Experimental Observation of Single-File Water Filling of Thin Single-Wall Carbon Nanotubes Down to Chiral Index (5, 3). *Phys. Rev. Lett.* **2010**, *104*, 207401.

(69) Machón, M.; Reich, S.; Telg, H.; Maultzsch, J.; Ordejón, P.; Thomsen, C. Strength of Radial Breathing Mode in Single-Walled Carbon Nanotubes. *Phys. Rev. B: Condens. Matter Mater. Phys.* **2005**, *71*, 035416.

(70) Gordeev, G.; Flavel, B.; Krupke, R.; Kusch, P.; Reich, S. Asymmetry of Resonance Raman Profiles in Semiconducting Single-Walled Carbon Nanotubes at the First Excitonic Transition. *Phys. Rev. B: Condens. Matter Mater. Phys.* **2019**, *99*, 045404.

(71) Bergler, F. F.; Stahl, S.; Goy, A.; Schöppler, F.; Hertel, T. Substrate-Mediated Cooperative Adsorption of Sodium Cholate on (6,5) Single-Wall Carbon Nanotubes. *Langmuir* **2016**, *32*, 9598–9603.

(72) Shastry, T. A.; Morris-Cohen, A. J.; Weiss, E. A.; Hersam, M. C. Probing Carbon Nanotube–Surfactant Interactions with Two-Dimensional DOSY NMR. *J. Am. Chem. Soc.* **2013**, *135*, 6750–6753.

(73) Hennrich, F.; Li, W.; Fischer, R.; Lebedkin, S.; Krupke, R.; Kappes, M. M. Length-Sorted, Large-Diameter, Polyfluorene-Wrapped Semiconducting Single-Walled Carbon Nanotubes for High-Density, Short-Channel Transistors. *ACS Nano* **2016**, *10*, 1888–1895.

(74) Li, W.-S.; Hou, P.-X.; Liu, C.; Sun, D.-M.; Yuan, J.; Zhao, S.-Y.; Yin, L.-C.; Cong, H.; Cheng, H.-M. High-Quality, Highly Concentrated Semiconducting Single-Wall Carbon Nanotubes for Use in Field Effect Transistors and Biosensors. *ACS Nano* **2013**, *7*, 6831–6839.

(75) Brady, G. J.; Jenkins, K. R.; Arnold, M. S. Channel Length Scaling Behavior in Transistors Based on Individual *versus* Dense Arrays of Carbon Nanotubes. *J. Appl. Phys.* **2017**, *122*, 124506.

(76) Fagan, J. Aqueous Two-Polymer Phase Extraction of Single-Wall Carbon Nanotubes using Surfactants. *Nanoscale Adv.* **2019**, *1*, 3307–3324.

(77) Fagan, J. A.; Zheng, M.; Rastogi, V.; Simpson, J. R.; Khripin, C. Y.; Silvera Batista, C. A.; Hight Walker, A. R. Analyzing Surfactant Structures on Length and Chirality Resolved (6, 5) Single-Wall Carbon Nanotubes by Analytical Ultracentrifugation. *ACS Nano* **2013**, *7*, 3373–3387.

(78) Lam, S.; Zheng, M.; Fagan, J. A. Characterizing the Effect of Salt and Surfactant Concentration on the Counterion Atmosphere Around Surfactant Stabilized SWCNTs Using Analytical Ultracentrifugation. *Langmuir* **2016**, *32*, 3926–3936.

(79) Schuck, P. Size-Distribution Analysis of Macromolecules by Sedimentation Velocity Ultracentrifugation and Lamm Equation Modeling. *Biophys. J.* **2000**, *78*, 1606–1619.

(80) Schuck, P. *Sedimentation Velocity Analytical Ultracentrifugation: Discrete Species and Size-Distributions of Macromolecules and Particles*; CRC Press: New York, 2016.

(81) Vijayaraghavan, A.; Blatt, S.; Weissenberger, D.; Oron-Carl, M.; Hennrich, F.; Gerthsen, D.; Hahn, H.; Krupke, R. Ultra-Large-Scale Directed Assembly of Single-Walled Carbon Nanotube Devices. *Nano Lett.* **2007**, *7*, 1556–1560.